

DETECTING SPATIAL HEALTH DISPARITIES USING DISEASE MAPS

BY LUCA AIELLO ^{1,*} AND SUDIPTO BANERJEE ²

¹*Department of Economics, Management and Statistics, University of Milano-Bicocca. *Laiello4@campus.unimib.it*

²*Department of Biostatistics, University of California, Los Angeles, sudipto@ucla.edu*

Epidemiologists commonly use regional aggregates of health outcomes to map mortality or incidence rates and identify geographic disparities. However, to detect health disparities across regions, it is necessary to identify “difference boundaries” that separate neighboring regions with significantly different spatial effects. This can be particularly challenging when dealing with multiple outcomes for each unit and accounting for dependence among diseases and across areal units. In this study, we address the issue of multivariate difference boundary detection for correlated diseases by formulating the problem in terms of Bayesian pairwise multiple comparisons by extending it through the introduction of adjacency modeling and disease graph dependencies. Specifically, we seek the posterior probabilities of neighboring spatial effects being different. To accomplish this, we adopt a class of multivariate areally referenced Dirichlet process models that accommodate spatial and inter-disease dependence by endowing the spatial random effects with a discrete probability law. Our method is evaluated through simulation studies and applied to detect difference boundaries for multiple cancers using data from the Surveillance, Epidemiology, and End Results Program of the National Cancer Institute.

1. Introduction. Health disparities, or inequities, broadly refer to sections of the population being deprived of fair and equal opportunities to seek healthcare (see, e.g., the recent text by [Rao, 2023](#)). Spatial disparities in health manifest in the form of variations in health outcomes over geographic regions and are often visually represented using disease maps ([Koch, 2005](#)). While the role of spatial data analysis in epidemiological investigations has been extensively documented (see, e.g., [Waller and Gotway, 2004](#); [Waller and Carlin, 2010](#); [Lawson, 2013](#); [Lawson et al., 2016](#), and further references therein), a specialized exercise of detecting “boundaries” or zones of abrupt change on disease maps is directly relevant to statistical detection of health disparities. In public health, such *difference boundaries*, or *wombling boundaries* (so called after a seminal paper by [Womble, 1951](#)), indicate significantly different disease mortality and incidence across regions, thereby improving decision-making for disease prevention and control, geographic allocation of health care resources, and so on (see [Jacquez and Greiling, 2003a,b](#); [Lu and Carlin, 2005](#); [Li, Banerjee and McBean, 2011](#); [Ma and Carlin, 2007](#); [Fitzpatrick et al., 2010](#), for some algorithmic approaches with applications). Model-based approaches aiming for full probabilistic uncertainty quantification have also received much attention and include, but are not limited to, developments in [Lu et al. \(2007\)](#); [Ma, Carlin and Banerjee \(2010\)](#); [Li et al. \(2015, 2012\)](#); [Hanson et al. \(2015\)](#); [Corpas-Burgos and Martinez-Beneito \(2020\)](#) and [Gao, Banerjee and Ritz \(2022\)](#).

This manuscript builds on the above developments in what may be described as still a fledgling area. We devise a probabilistic learning mechanism for adjacency boundaries on a map when such information may become available. An administrative or political boundary

Keywords and phrases: Bayesian hierarchical models, Difference Boundary Analysis, Disease mapping, False discovery rates, Spatial Dirichlet Processes, Spatial epidemiology.

separating two adjacent regions need not delineate them in terms of the health outcomes measured there. In fact, in disease mapping and spatial smoothing of areal data the customary approach is to assume that neighboring regions are similar to each other. This assumption runs counter to detecting health disparities, where we seek out differences and not similarities. Therefore, modeling spatial disparities needs to balance underlying processes generating similarities based upon geographic proximity with processes generating significant differences between neighbors. We specifically pursue an effective manner of modeling the adjacency relations on a map. Our contribution is summarized in the context of the two broad themes. The first builds stochastic models for the adjacency matrices (Lu et al., 2007; Ma, Carlin and Banerjee, 2010; Lee and Mitchell, 2012; Corpas-Burgos and Martinez-Beneito, 2020) that, in principle, can accommodate information from explanatory variables in ascertaining the presence of edges. Based upon the complexity of the resulting models and numerical difficulties in estimating such edges, a different approach forgoes introducing variables in the adjacency, but detects edges using multiple comparisons by estimating the spatial random effects and, subsequently, testing how many such pairs are significantly different. A Bayesian approach (Li et al., 2015, 2012; Gao, Banerjee and Ritz, 2022) holds appeal as the posterior distribution of spatial effects produce an exact Bayesian false discovery rate (FDR) (Müller et al., 2004) without recourse to asymptotic assumptions that are inappropriate in areal settings.

We offer a framework that melds the two themes. We build upon the recent developments in Gao, Banerjee and Ritz (2022) by embedding directed acyclic graphical autoregression (DAGAR) models (Datta et al., 2019) within a hierarchical Bayesian nonparametric model. This nonparametric specification is critical as it introduces discrete probability masses on the spatial random effects and allows us to meaningfully calculate the posterior probabilities of two neighboring spatial effects being equal. This sets up boundary detection using Bayesian FDR. We further enrich the model by allowing the DAGAR adjacency matrix to learn from explanatory variables that may carry information regarding whether two neighboring regions are similar. Thus, each element of a binary adjacency matrix is modeled using an exponential threshold devised by Lee and Mitchell (2012). We develop joint models for multiple diseases (cancers), where the diseases are dependent and accommodate disease-specific learning of adjacency relationships. We allow difference boundaries to vary by health outcomes and explain the impact of explanatory variables on such boundaries. Here, we consider unstructured disease dependencies and those posited by conditional dependencies in graphical models.

The data analytic merits of our proposed approach are best appreciated in comparison to approaches that adhere to one, but not both, of the boundary detection themes discussed above. Methods that allow uncertainty through purely parametric adjacency relations (including regression models for adjacency matrices) within widely used conditional autoregression models often encounter numerical difficulties in convergence of iterative estimation algorithms, such as Markov chain Monte Carlo (MCMC). On the other hand, methods offering FDR based boundary detection without allowing adjacency learning from explanatory variables can lead to inflated detection rates of boundaries by failing to account for additional uncertainties in adjacency relations. We demonstrate this phenomenon in the cancer boundary detection rates reported recently by Gao, Banerjee and Ritz (2022).

The balance of our article proceeds as follows. Section 2 describes the data we subsequently analyze. This data, extracted from the National Cancer Institute’s (NCI) Surveillance Epidemiology and End Results (SEER) database records occurrences of four different cancer types across the counties of California together with explanatory variables for modeling outcomes and boundaries. Section 3 develops our proposed multivariate Bayesian modeling framework using an areal stick-breaking process with a DAGAR spatial distribution with unknown boundaries as its baseline measure. Section 4 presents a suite of simulation experiments to elicit insights into the performance of our proposed model using various metrics. Section 5 applies spatial boundary detection to the data set described in Section 2 and we conclude with some remarks in Section 6. Additional materials are provided in the Appendix.

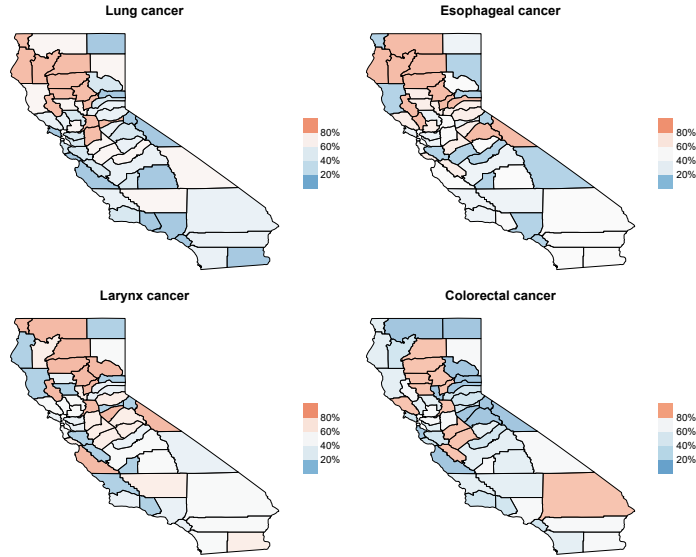


Fig 1: Maps of age-sex adjusted standardized incidence ratios (SIR) for lung, esophageal, larynx, and colorectal cancer in California, 2012–2016.

2. Data. We explore an areal data set extracted from the SEER*Stat database using the SEER*Stat statistical software (National Cancer Institute, 2019). The data records the occurrence of four potentially interrelated types of cancers: lung, esophageal, larynx, and colorectal. The occurrences of these cancers are aggregated from January 2012 through December 2016 and presented as counts in each of the 58 counties of California. Previous research has shown that lung and esophageal cancers share common risk factors (Agrawal, Markert and Agrawal, 2018) and metabolic mechanisms (Shi and Chen, 2004). Furthermore, it has been found that lung cancer is one of the most frequent second primary cancers in patients with colon cancer (Kurishima et al., 2018). Patients with laryngeal cancer are also at a high risk of developing second primary lung cancer (Akhtar et al., 2010). Hence, we seek to account for the dependence between the cancers due to non-spatial factors.

Let (y_{id}) be the observed counts for cancer type d ($d = 1, 2, 3, 4$) in county i ($i = 1, 2, \dots, 58$). Our model, developed in Section 3, accounts for the expected number of cases (E_{id}) by adjusting for age-sex demographics in each county. Specifically, we calculate the expected age-sex adjusted number of cases in county i for cancer d as $E_{id} = \sum_{k=1}^m c_d^k N_i^k$ (Jin, Carlin and Banerjee, 2005), where $c_d^k = (\sum_{i=1}^{58} y_{id}^k) / (\sum_{i=1}^{58} N_i^k)$ is the age-sex specific incidence rate in age-sex group k for cancer d across all California counties; y_{id}^k represents the incidence count in age-sex group k of county i for cancer d , and N_i^k represents the population in age-sex group k of county i . The age groups have been determined based on 5-year intervals up to 85 years or older. These age intervals are as follows: less than 1 year, 1–4 years, 5–9 years, 10–14 years, and so on, up to 80–84 years and 85+ years. This results in a total of $m = 19 \times 2 = 38$ age-sex groups.

Figure 1 displays a map of California’s counties, illustrating the age-sex adjusted standardized incidence ratios ($SIR_{id} = y_{id}/E_{id}$) for different types of cancer. The SIR values are classified into quintiles, and distinct thresholds are established for each level of SIRs. The map reveals a notable pattern, where regions exhibiting comparable SIRs tend to cluster together geographically, forming distinct groups. This clustering is evident in the group of regions with the highest incidence rates for each cancer. The high SIR values for all of the cancer types are concentrated in northern counties, with the only exception being that

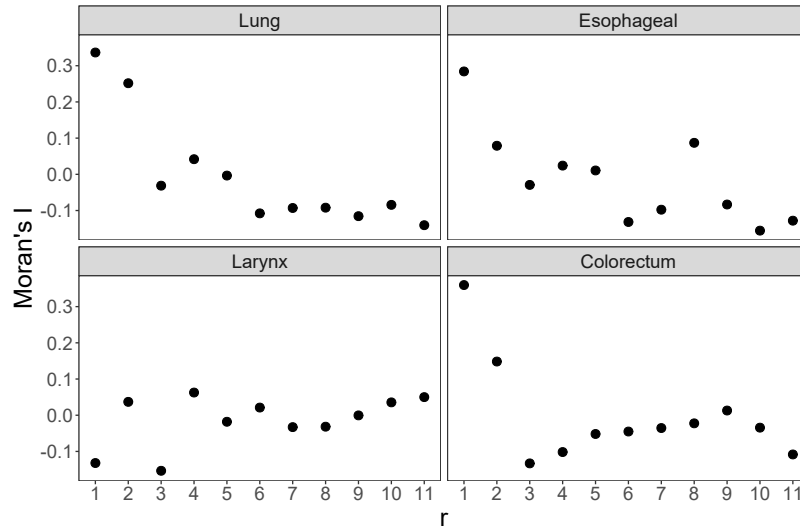


Fig 2: Moran's I of r -th order neighbors for lung, esophageal, larynx, and colorectal cancer.

of a high SIR for colorectal cancer in a southern county (San Bernardino). Additionally, in northern counties, we notice that several counties with high SIRs are situated next to areas with low SIRs. Our proposed model, which detects boundaries, provides a robust, adaptable, interpretable and clear analytical tool for identifying these geographical clusters.

We used Pearson's correlation coefficient as an exploratory tool to evaluate the relationships between various types of cancers. In a preliminary analysis, we treated the SIRs from different counties as independent samples. Our findings indicate a significant association in the incidence of lung cancer with each of esophageal (correlation coefficient 0.58), larynx (0.40), and colorectal (0.50) cancers. We also measured a correlation coefficient of 0.42 between esophageal and larynx cancer. Moreover, to assess the spatial relationships of each cancer type, we employed the Moran's I statistic, which was computed based on the r -th order neighbors for each cancer. These calculations were then used to generate an areal correlogram, as described by [Banerjee, Carlin and Gelfand \(2014\)](#). In our analysis, we defined distance intervals as $(0, d_1], (d_1, d_2], (d_2, d_3], \dots$, with the r -th order neighbors referring to units that fall within the distance range of $(d_r - 1, d_r]$, and indicating that they are separated by a distance greater than $d_r - 1$ but within a distance of d_r . The distance measure we used was the Euclidean distance derived from an Albers map projection of California. Figure 2 presents the results of our correlation analysis, which shows the spatial associations for lung, esophageal, colorectal, and larynx cancers. It is clear that as the order of neighbors (r) increases, the spatial associations diminish notably for lung, esophageal, and colorectal cancers. However, the observed pattern is less pronounced and clear for larynx cancer.

To provide a comprehensive analysis and explain the impact of risk factors, we incorporate covariates into our model to capture both the mean structure and identify neighboring areas with significant differences in rates. A detailed analysis is presented in Section 5. In Figure 3, we display the smoking, over 65, and below poverty threshold rates for each county, arranged from left to right. These plots reveal notable patterns: the northern counties exhibit a higher concentration of smoking rates, with a few exceptions in the central counties; both northern and eastern counties have higher rates of individuals over 65; and the northern and central counties have higher rates below the poverty threshold. Conversely, the coastal regions demonstrate relatively lower rates across all the covariates, indicating a distinct contrast between different geographical areas (see [Doll et al., 2005](#), for similar findings). Interestingly,

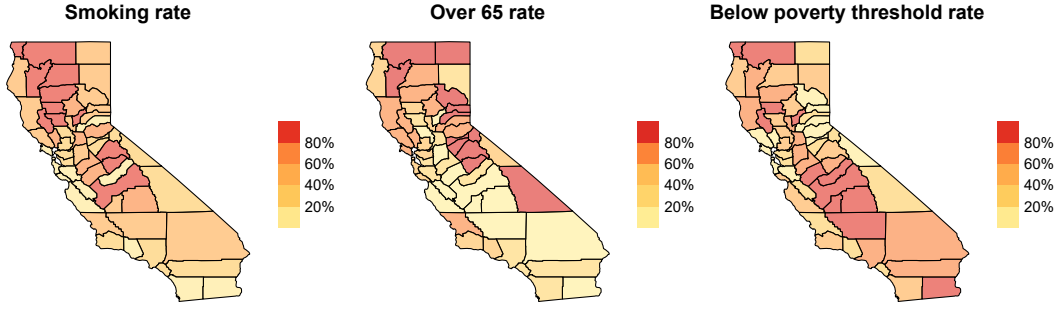


Fig 3: Maps of county-level covariates

central and southern counties exhibit lower rates specifically in the over 65 variable. The significance and implications of these findings will be discussed in greater detail in Section 5.

3. Model development. We construct a generalized linear mixed model for the disease outcome, y_{id} , using a distribution from the exponential family with a canonical link,

$$(1) \quad g(E(y_{id})) = \mathbf{x}_{id}^T \boldsymbol{\beta}_d + \phi_{id},$$

for each areal unit $i = 1, \dots, n$ and disease $d = 1, \dots, q$. The large scale trend is modeled using a regression, where \mathbf{x}_{ij} is a vector of explanatory variables and $\boldsymbol{\beta}_d$ is the corresponding vector of slopes, while ϕ_{id} is the spatial random effect for disease d in region i . For detecting difference boundaries, we seek $P(\phi_{id} \neq \phi_{jd} | \mathbf{y}, i \sim j)$, where \mathbf{y} is the collection of observed y_{id} 's and $i \sim j$ means that regions i and j are neighbors. This raises an issue about the prior distribution for the ϕ_{id} 's. A continuous probability distribution is inappropriate because the resulting posterior probability is $P(\phi_{id} \neq \phi_{jd} | \mathbf{y}, i \sim j) = 1$, which leads to all n boundaries being detected. This limitation highlights the need for a model that accounts for spatial dependence while assigning discrete probability masses on spatial random effects. Such a model enables including non-zero probabilities for the random effects being equal. Indeed, our approach will ensure non-null probabilities of equality between the random effects, resulting in a smaller number of boundaries detected compared to n . The Dirichlet Process (DP) offers a natural way to cluster regions, as it ensures that $P(\phi_{id} = \phi_{jd} | \mathbf{y}, i \sim j) > 0$. Moreover, it presents a versatile framework for capturing the spatial effects represented by ϕ_{id} . The model below belongs to a subclass of stick-breaking process priors and includes the DP as a special instance.

3.1. Spatial random effects. Let $\boldsymbol{\phi} = (\phi_1^T, \dots, \phi_q^T)^T$ be the $N \times 1$ vector, where $N = nq$ and $\phi_d = (\phi_{1d}, \dots, \phi_{nd})^T$ for each $d = 1, \dots, q$. Following [Gao, Banerjee and Ritz \(2022\)](#) we let $\{1, \dots, n, \dots, (q-1)n+1, \dots, N\}$ be an enumeration of the pairwise (i, d) indices corresponding to the ordering of $\boldsymbol{\phi}$, thereby dealing with a unique $N \times 1$ vector $\boldsymbol{\phi}$. We let $\boldsymbol{\phi} \sim G_N$, where G_N is an unknown distribution further specified by $G_N = \sum_{u_1, \dots, u_N} \pi_{u_1, \dots, u_N} \delta_{\theta_{u_1}, \dots, \theta_{u_N}}$, where

$$(2) \quad \pi_{u_1, \dots, u_N} = P \left(\sum_{k=1}^{u_1-1} p_k < F^{(1)}(\gamma_1) < \sum_{k=1}^{u_1} p_k, \dots, \right. \\ \left. \dots \sum_{k=1}^{u_N-1} p_k < F^{(N)}(\gamma_N) < \sum_{k=1}^{u_N} p_k \right); \quad \boldsymbol{\gamma} \sim \mathcal{N}_N(\mathbf{0}, \boldsymbol{\Sigma}_\boldsymbol{\gamma}),$$

where $\theta_k | \tau_s \stackrel{iid}{\sim} \mathcal{N}(0, 1/\tau_s)$ for $k = 1, \dots, K$. The motivation behind the choice of the independent and identically distributed assumption for the atoms base distribution stems from the necessity of establishing ties across both regions and cancers. For instance, if we were to assign different means to different cancers, we could still accommodate ties within each cancer, wherein different regions' random effects assume the same value. However, we would be unable to establish ties across cancers, as the underlying distribution from which the atoms are sampled would differ.

Priors for model parameters are specified as $\beta_d \stackrel{iid}{\sim} \mathcal{N}(\mathbf{0}, \Sigma_{\beta_d})$, while the precision (inverse variance) parameter $1/\tau_s \sim IG(a_s, b_s)$, where a_s is shape and b_s is scale. We specify the stick-breaking weights by $p_1 = V_1$ and $p_j = V_j \prod_{k < j} (1 - V_k)$ for $j = 2, \dots, K$, where $V_k \stackrel{iid}{\sim} Beta(1, \alpha)$. Moreover, u_1, \dots, u_N are indices of the elements of $\theta = (\theta_1, \dots, \theta_N)^T$ sampled for the N observations, δ_θ is the Dirac measure located at θ , and $F^{(1)}(\cdot), \dots, F^{(N)}(\cdot)$ are cumulative distribution functions of the marginal distribution of the corresponding γ elements, indexed in accordance with the elements of ϕ .

The weights in the distribution G_N are constructed by utilizing the marginal cumulative distribution function (CDF) of the elements of γ . This construction combines two approaches: the hybrid Dirichlet process (Petroni, Guindani and Gelfand, 2009), which involves the use of point-referenced continuous spatial copulas to model weight dependency, and the latent stick-breaking process (Rodríguez, Dunson and Gelfand, 2010), which employs ordered atoms. Marginally, each $F^{(i)}(\gamma_i)$ is $\mathcal{U}(0, 1)$ but they are dependent through the γ_i , and the distribution of each spatial random effect ϕ_i is a regular univariate DP, with the spatial dependence between these DPs introduced using a copula representation for the weights. In theory, $K = \infty$ yields a fully non-parametric model, but we follow the standard practice of replacing the infinite sum with the sum of the initial K ($K \leq n$) terms, as the probability masses diminish rapidly. Should concerns about truncation bias arise, an alternative method called slice-sampling (described in Kalli, Griffin and Walker, 2011) is available for exact sampling. In particular, for areal data the value of K is naturally constrained by the number of areal units rendering the infinite representation redundant.

The marginal covariance between two spatial random effects ϕ_i and ϕ_j where, in this case, $i, j = 1, \dots, N$, can be expressed as

$$(3) \quad \text{Cov}(\phi_i, \phi_j) = \frac{b_s}{a_s - 1} \sum_{k=1}^K \pi_{kk}^{(i,j)}$$

where

$$(4) \quad \pi_{kk}^{(i,j)} = P \left(\sum_{t=1}^{k-1} p_t < F^{(i)}(\gamma_i) < \sum_{t=1}^k p_t, \sum_{t=1}^{k-1} p_t < F^{(j)}(\gamma_j) < \sum_{t=1}^k p_t \right)$$

Equation (3) and (4) evinces how the spatially dependent elements of γ induce associations among the elements of ϕ . The covariance of ϕ also depends on the hyperparameters of the precision parameter prior of the base distribution. Higher values of the probabilities, i.e., $\pi_{kk}^{(i,j)}$, produce higher correlation between the random effects. Unsurprisingly, a higher likelihood of ϕ_i and ϕ_j exhibiting similar values implies a higher covariance in (3). We next attend to modeling the spatial covariance matrix Σ_γ .

3.2. DAGAR with adjacency modeling. DAGAR uses a fixed set of arbitrarily ordered regions yielding a *topologically ordered* set of vertices, $\mathcal{V} = \{1, \dots, n\}$, and a set \mathcal{E} of directed edges that encode “neighbors” of every region. Rather than defining all geographically adjacent regions as neighbors, DAGAR defines neighbors of a given region i as regions that (i)

are geographically adjacent to i ; AND (ii) precede i in the topological order. The directed graph $\mathcal{G} = (\mathcal{V}, \mathcal{E})$ is constructed from this definition. The precision matrix of a DAGAR random variable is $\mathbf{Q}(\rho) = (\mathbf{I} - \mathbf{B})^\top \mathbf{\Lambda} (\mathbf{I} - \mathbf{B})$, where $\mathbf{B} = (b_{ij})$ is $n \times n$ with elements $b_{ij} = \frac{\rho}{1+(n_{<i}-1)\rho^2}$ if there is a directed edge $(i, j) \in \mathcal{E}$ for $i \geq 2$, where $n_{<i}$ is the number of neighboring regions preceding i , and $b_{ij} = 0$ if $(i, j) \notin \mathcal{E}$. In DAGAR, $(i, j) \in \mathcal{E}$ if $j < i$ in the topological order and regions i and j are geographically adjacent. This implies that $b_{ii} = 0$ and $b_{ij} = 0$ for all $i \leq j$ so \mathbf{B} is strictly lower triangular. The $n \times n$ diagonal matrix $\mathbf{\Lambda} = \text{diag}(\lambda_i)$ has elements $\lambda_i = \frac{1+(n_{<i}-1)\rho^2}{1-\rho^2}$ along its diagonal for $i = 1, \dots, k$, where $n_{<1} = 0$. Datta et al. (2019) show that ρ is a direct indicator of spatial autocorrelation. DAGAR holds further appeal as it accounts for all edges without any omissions, while still yielding a computationally efficient precision matrix.

Two extensions to the DAGAR are relevant to our current inferential objectives. First, as articulated in Section 1, we intend to model the adjacency matrix rather than specifying it purely from the map. Geographic adjacency, by itself, need not be enough to infer similarities or disparities and we accommodate learning about the adjacency relations using risk factors or other explanatory variables. We thereby recognize that inferring about spatial disparities relies upon effectively estimating difference boundaries. We exploit the available data on spatially oriented risk factors and explanatory variables to drive inference on difference boundaries. Second, while extending the model to jointly model dependent cancer occurrences, we allow the impact of the factors informing about the edges to vary by the diseases under considerations. This results in an effective amalgamation of the approach in Lee and Mitchell (2012) with that in Gao, Banerjee and Ritz (2022).

3.2.1. *Adjacency modeling.* Unlike in more traditional spatial autoregression models, such as simultaneous and conditional autoregression (SAR and CAR, respectively), where the precision matrix includes an adjacency matrix whose elements can be modeled using explanatory variables (Lu et al., 2007), the elements of the DAGAR precision matrix, b_{ij} , are specified in a manner that renders ρ as a spatial correlation parameter. It is, therefore, unapparent how information from explanatory variables, predictors or risk factors can be introduced in the adjacency. In order to achieve this, we construct a strictly lower triangular $n \times n$ adjacency matrix, $\mathbf{W} = (w_{ij})$ based upon the fixed topological order of regions to assimilate information from preceding neighboring regions. This results in $w_{ij} = 0$ for $i \leq j$ or $i \not\sim j$, where $i \sim j$ indicates ‘‘neighbors’’ as defined in the preceding section. Note that \mathbf{W} encodes all of the information contained in the original DAGAR. Thus, for each region i its preceding neighbors are contained in $\{j : j < i, j \sim i\} \equiv \{j : w_{ij} = 1\}$. Subsequently, we introduce \mathbf{W} into the DAGAR precision matrix as

$$(5) \quad \mathbf{Q}(\rho, \mathbf{W}) = (\mathbf{I} - \mathbf{B})^\top \mathbf{\Lambda} (\mathbf{I} - \mathbf{B}); \quad \text{where} \quad \mathbf{B} = \tilde{\mathbf{B}} \circ \mathbf{W},$$

where $\tilde{\mathbf{B}} = (\tilde{b}_{ij})$ with elements $\tilde{b}_{ij} = \frac{\rho}{1+(n_{<i}-1)\rho^2}$, $\lambda_i = \frac{1+(n_{<i}-1)\rho^2}{1-\rho^2}$, $n_{<i} = \sum_{j=1}^n w_{ij}$ and \circ denotes the Hadamard (or elementwise) product.

The matrix $\tilde{\mathbf{B}}$ is dense with all its elements being possibly non-zero. However, $\tilde{\mathbf{B}} \circ \mathbf{W}$ retains the sparse lower-triangular structure characteristic of DAGAR. Instead of directly setting the non-null elements of \mathbf{W} to fixed values, one possibility is to model each element of \mathbf{W} as a separate random quantity. For instance, Lu et al. (2007) employed a logistic model for the elements of a symmetric adjacency matrix in a CAR model while considering boundary-specific risk factors. In our DAGAR setting, a parallel approach would be to model the lower triangular elements $w_{ij} | p_{ij} \stackrel{\text{ind}}{\sim} \text{Bernoulli}(p_{ij})$ and introducing a regression model in, for example, a logistic link $\log(p_{ij}/(1-p_{ij}))$. Other possible approaches include adapting

random adjacency models, such as in [Ma, Carlin and Banerjee \(2010\)](#), to DAGAR by leveraging an Ising model for elements of \mathbf{W} . However, the information needed to estimate such models is rarely available and require informative prior distributions resulting in excessively parametrized covariance models for γ that inaccurately estimate uncertainties and produce biased inference for spatial boundaries (also see [Li, Banerjee and McBean, 2011](#), who argue that effectively modeling geographical adjacency would require a separate parameter for every pair of neighbors resulting in overparametrized models).

In what follows, we adopt a simpler and more effective approach based on [Lee and Mitchell \(2012\)](#), following who we model the adjacency matrix as

$$(6) \quad w_{ij}(\boldsymbol{\eta}) = \begin{cases} 1 & \text{if } \exp(-\mathbf{z}_{ij}^T \boldsymbol{\eta}) \geq 0.5 \text{ and } i \sim j \\ 0 & \text{otherwise,} \end{cases}$$

where \mathbf{z}_{ij} consist of explanatory variables specific to pairs of regions i and j and are assumed to be non-negative in each element. In practice, they could represent an absolute measure of discrepancy between the two regions with $\boldsymbol{\eta}$ being the vector of corresponding coefficients. Equation (6) encodes geographic neighbors so as to not represent disparities whenever $\mathbf{z}_{ij}^T \boldsymbol{\eta} \leq \log 2$. Furthermore, \mathbf{z}_{ij} excludes an intercept so regions with homogeneous populations, i.e., $\mathbf{z}_{ij} = \mathbf{0}$, are deemed adjacent. The coefficients in $\boldsymbol{\eta}$ act as disparity parameters and are assumed to be nonnegative with each element assigned a Uniform prior distribution between 0 and a fixed positive constant such that at most 50% of geographic neighbors in the study region are classified as difference boundaries. Higher values in $\boldsymbol{\eta}$ assist in exceeding the threshold, which results in a loss of a geographical boundary in \mathbf{W} to be smoothed over and, hence, indicating a spatial disparity.

A salient feature of the preceding development is the assimilation of information from explanatory variables \mathbf{x}_{id} in (1) and \mathbf{z}_{ij} in (6). The former informs about the observed values of the health outcomes and captures large scale trends, while the latter provides information on disparities among geographic neighbors. The vectors \mathbf{x}_{id} and \mathbf{z}_{ij} could include the same variables but need to be indexed differently. For example, one could include the smoking rate for a region i in \mathbf{x}_{id} and the difference in smoking rates between regions i and j in \mathbf{z}_{ij} . While the slope β is interpreted as in the customary generalized linear models with exponential families, the coefficients in $\boldsymbol{\eta}$ indicate whether the corresponding variable in \mathbf{z}_{ij} signifies a disparity or not. In particular, a smaller value of a coefficient η_k indicates the k -th variable in \mathbf{z}_{ij} . For example, they can be map-based, such as the distance between the centroids of regions i and j or the discrepancies in the percentage of common boundaries shared by the two regions compared to their total geographical boundaries. Auxiliary topological data may be relevant, such as the presence of challenging natural features like mountain ranges or rivers that hinder travel between the regions. Our approach assimilates sociodemographic information into \mathbf{z}_{ij} . This involves comparing the percentages of urban area between the two regions or calculating the standardized absolute difference in a specific regional characteristic, such as the proportion of residents who smoke or even the expected age-adjusted disease count for the region. By including these covariates in \mathbf{z}_{ij} , the model can account for various factors that may influence the neighboring relationship between regions i and j .

In this way the covariance structure of γ exhibits a dual advantage: it is fully automatic and parsimonious, and yet it enables the data to determine the number and locations of any adjacency, rather than relying on the investigator's prior knowledge. Furthermore, we are introducing an exploratory tool in the proposed model, that assists investigators in comprehending the localized spatial patterns of disease risk. For instance, in cases where a adjacency is identified despite an observable discontinuity in the data, researchers can delve deeper into the areas in question to investigate other potential factors contributing to this discontinuity.

3.3. *Multivariate framework.* Recalling that our current data analytic goals involve accounting for dependence among multiple diseases and spatial dependence for each cancer, we turn to a rich literature on multivariate areal models (Mardia, 1988; Gelfand and Vounatsou, 2003; Carlin and Banerjee, 2003; Jin, Carlin and Banerjee, 2005; Jin, Banerjee and Carlin, 2007; Zhang, Hodges and Banerjee, 2009; Banerjee, 2016; MacNab, 2018; Gao, Datta and Banerjee, 2022). Following recent developments in Gao, Datta and Banerjee (2022) and Gao, Banerjee and Ritz (2022), who demonstrated advantages of the DAGAR model (Datta et al., 2019) with regard to overall model performance and interpretation of spatial correlation, we let γ follow a multivariate DAGAR (MDAGAR) model.

We introduce dependence among outcomes using linearly transformed latent variables resulting in an unstructured graph (left panel of Figure 4). Therefore, $\gamma_1 = a_{11}\mathbf{f}_1$, $\gamma_d = a_{d1}\mathbf{f}_1 + \dots + a_{dd}\mathbf{f}_d$ for each $d = 2, \dots, q$, where a_{dh} , $h = 1, \dots, d$, are unknown coefficients that associate spatial components for different diseases and each $\mathbf{f}_d \stackrel{ind}{\sim} \mathcal{N}(\mathbf{0}, \mathbf{Q}(\rho_d, \mathbf{W}_d)^{-1})$, where \mathbf{W}_d is a spatial adjacency matrix and ρ_d is the spatial autocorrelation parameter for disease d . Therefore, each γ_d is a linear combination of independent DAGAR random variables. This construction makes the model independent on the disease ordering because the association among the diseases is modeled using $\mathbf{A}\mathbf{A}^T$, where \mathbf{A} is the lower-triangular matrix with elements a_{dh} . The covariance matrix of γ is

$$(7) \quad \Sigma_\gamma = (\mathbf{A} \otimes \mathbf{I}_N) \left[\bigoplus_{d=1}^q \mathbf{Q}(\rho_d, \mathbf{W}_d)^{-1} \right] (\mathbf{A}^T \otimes \mathbf{I}_N)$$

where \otimes denotes the Kronecker product and \mathbf{W}_d is specified through (6) with a different η_d for each disease d . Therefore, we are incorporating a random adjacency matrix into the model for each type of cancer. We evaluate the model's performance by accounting for the particular cancer under consideration, as well as the explanatory variables utilized in model (6) that informs the adjacency structure, potentially varying for each cancer type.

We model $\mathbf{A}\mathbf{A}^T$ using an inverse-Wishart distribution with \mathbf{A} identifying as the unique lower-triangular Cholesky factor. Alternatively, we introduce a graphical model for the diseases as a representation of multivariate dependencies (see, e.g., Cox and Wermuth, 1993, 1996). Such models distinguish between directed and "undirected" graphs (central and right panels in Figure 4, respectively). The former assumes a topological ordering of the diseases, while the latter does not. For a directed graph, we build an inter-disease DAGAR using the ordering of the diseases and the adjacency matrix of the directed inter-disease graph. This amounts to modeling $\mathbf{A} = (\mathbf{I}_q - \mathbf{B})^{-1}\boldsymbol{\Lambda}^{-1/2}$ in (7), where $\mathbf{B} = (b_{ij})$ and $\boldsymbol{\Lambda} = (\lambda_i)$ are as defined in Section 3.2, but with \mathbf{W} using the inter-disease graph. This inter-disease DAGAR depends upon ordering of the diseases. Gao, Datta and Banerjee (2022) devised model choice and Bayesian model averaging over all topological orders in directed graphical models, but the approach is computationally onerous.

Consider a fixed directed acyclic disease graph $\mathcal{G}_{dis} = \{\mathcal{V}_{dis}, \mathcal{E}_{dis}\}$ (the suffix *dis* serves to distinguish this from the graph of the spatial map), where \mathcal{V}_{dis} is a set of q nodes and \mathcal{E}_{dis} is a set of directed edges from parent nodes to children (central panel of Figure 4 with $q = 4$). Let

$$(8) \quad \gamma_1 = \mathbf{f}_1, \quad \gamma_d = \mathbf{A}_{d,1}\gamma_1 + \dots + \mathbf{A}_{d,d-1}\gamma_{d-1} + \mathbf{f}_d, \quad \text{for } d = 2, \dots, q,$$

where each $\mathbf{f}_d \stackrel{ind}{\sim} \mathcal{N}(\mathbf{0}, \mathbf{Q}(\rho_d, \mathbf{W}_d)^{-1})$ and $\mathbf{A}_{d,d'}$ is $n \times n$ with $\mathbf{A}_{d,d'} = \mathbf{O}$ whenever $d' \geq d$. The linear equations in (8) encode the conditional distributions $p(\gamma_d | \gamma_1, \dots, \gamma_{d-1})$ for $d = 2, \dots, q$. Setting $\mathbf{A}_{d,d'} = \mathbf{O}$ whenever node d' is not a parent of d , i.e., there is no directed edge from d' to d , ensures that the model conforms to the conditional independence among diseases posited in \mathcal{G}_{dis} . If $\mathbf{A} = (\mathbf{A}_{d,d'})$ is the $N \times N$ block matrix with the $n \times n$ matrix $\mathbf{A}_{d,d'}$

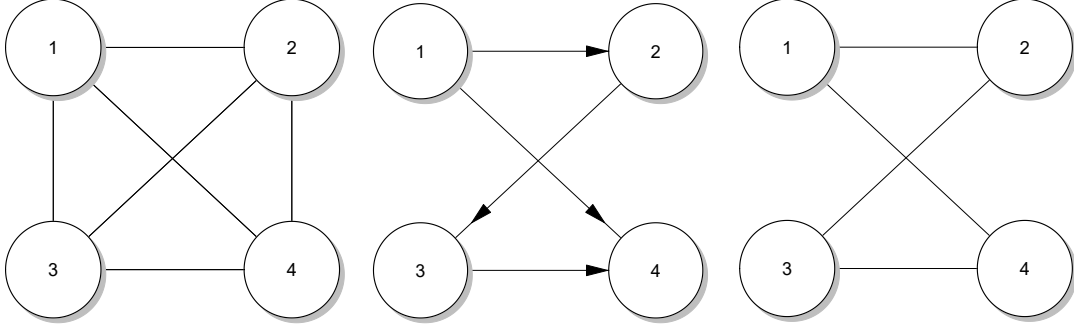


Fig 4: Left: unstructured graph, Center: directed acyclic graph. Right: undirected graph.

occupying block (d, d') , then \mathbf{A} is strictly lower triangular, hence $\mathbf{I}_N - \mathbf{A}$ is nonsingular and $\Sigma_\gamma = (\mathbf{I}_N - \mathbf{A})^{-1} [\bigoplus_{d=1}^q \mathbf{Q}(\rho_d, \mathbf{W}_d)^{-1}] (\mathbf{I}_N - \mathbf{A}^\top)^{-1}$ is positive definite no matter how we specify $\mathbf{A}_{d,d'}$ for all $(d, d') \in \mathcal{E}_{dis}$, i.e, d' is a parent of d .

Setting $\mathbf{A}_{d,d'} = \alpha_{0dd'} \mathbf{I}_n + \alpha_{1dd'} \mathbf{W}$, where \mathbf{W} is the fixed geographic map, introduces parameters $\alpha_{0dd'}$ and $\alpha_{1dd'}$ that allow the nature of dependence between diseases d and d' to vary across space. This flexibility is desirable because inter-disease dependencies, or lack thereof, are often manifestations of lurking shared risk factors that remain unaccounted for.

In contrast to directed acyclic graphs, “undirected” graphs model relationships among nodes using conditional dependencies. An edge between nodes signifies conditional dependence given all other nodes, while the absence of an edge indicates conditional independence given all other nodes (right panel in Figure 4 with $q = 4$). Given an undirected disease graph, we adapt a multivariate conditional autoregression model (MCAR, [Mardia, 1988](#); [Carlin and Banerjee, 2003](#); [Gelfand and Vounatsou, 2003](#)) by specifying the full conditional models,

$$(9) \quad \gamma_d | \gamma_{(-d)} \sim \mathcal{N}_n \left(\sum_{h=1}^q \mathbf{A}_{d,h} \gamma_h, \mathbf{Q}(\rho_d, \mathbf{W}_d)^{-1} \right),$$

where, $\gamma_{(-d)}$ represents the collection of all random effects except for the d -th disease type. The matrices $\mathbf{A}_{d,h}$ represent $n \times n$ matrices that encode the relationships between various cancers, while $\mathbf{Q}(\rho_d, \mathbf{W}_d)$ refers to the univariate precision matrix of the DAGAR model applied to the d -th cancer, capturing the spatial correlation within each cancer case. By exploiting a multivariate extension of Brook’s Lemma (see, e.g., [Mardia, 1988](#); [Banerjee, Carlin and Gelfand, 2014](#)), the collection of distributions in (9) yield the following joint distribution:

$$(10) \quad p(\gamma) \propto \exp \left(-\frac{1}{2} \gamma^\top \Sigma_\gamma^{-1} \gamma \right)$$

where $\Sigma_\gamma^{-1} = \mathbf{M}^{-1} (\mathbf{I}_N - \mathbf{A})$, $\mathbf{M}^{-1} = \bigoplus_{d=1}^q \mathbf{Q}(\rho_d, \mathbf{W}_d)$, and, analogously to the previous case, $\mathbf{A} = (\mathbf{A}_{d,h})$ is the $N \times N$ block matrix with the $n \times n$ matrix $\mathbf{A}_{d,h}$ occupying the (d, h) -th block. The key consideration here is to ensure that Σ_γ^{-1} is positive definite.

Let $\Lambda_{dis} = (\mathbf{D}_{dis} - \rho_{dis} \mathbf{W}_{dis})$ be $q \times q$, where \mathbf{W}_{dis} is the $q \times q$ binary adjacency matrix of the inter-disease graph, \mathbf{D}_{dis} is diagonal with the number of edges incident on each node as its diagonal element, and $\rho_{dis} \in (1/\zeta_{min}, \zeta_{max})$ with $\zeta_{min} < 0$ and $\zeta_{max} = 1$ denoting the smallest and largest eigenvalues of $\mathbf{D}_{dis}^{-1/2} \mathbf{W}_{dis} \mathbf{D}_{dis}^{-1/2}$, respectively; all eigenvalues are real, $\zeta_{max} = 1$ since $\mathbf{D}_{dis}^{-1} \mathbf{W}_{dis}$ is row-stochastic and $\zeta_{min} < 0$ since the trace of $\mathbf{D}_{dis}^{-1/2} \mathbf{W}_{dis} \mathbf{D}_{dis}^{-1/2}$ is zero. The interval for ρ_{dis} ensures that Λ_{dis} is positive definite. Let $\mathbf{R}_d^\top \mathbf{R}_d = (1/\lambda_{dis,dd}) \mathbf{Q}(\rho_d, \mathbf{W}_d)$ with $\sqrt{\lambda_{dis,dd}} \mathbf{R}_d$ being the upper-triangular Cholesky factor of $\mathbf{Q}(\rho_d, \mathbf{W}_d)$. Setting $\mathbf{A}_{dh} = (\lambda_{dis,dh}/\lambda_{dis,dd}) \mathbf{R}_d^{-1} \mathbf{R}_h$ yields

$\Sigma_\gamma^{-1} = (\oplus_{d=1}^q \mathbf{R}_d^T) (\mathbf{\Lambda}_{dis} \otimes \mathbf{I}) (\oplus_{d=1}^q \mathbf{R}_d)$, which is positive definite. Hence, (10) is a proper prior distribution for the spatial effects incorporating spatial autocorrelation using DAGAR and conforming to a posited undirected conditional independence graph.

3.4. *Model implementation.* Letting $\boldsymbol{\eta} = (\boldsymbol{\eta}_1^T, \dots, \boldsymbol{\eta}_q^T)^T$, and $\boldsymbol{\beta}$ defined analogously, for the unstructured disease graph we evaluate the following joint posterior distribution,

$$(11) \quad p(\boldsymbol{\theta}, \boldsymbol{\beta}, \tau_s, \mathbf{V}, \boldsymbol{\gamma}, \boldsymbol{\rho}, \boldsymbol{\eta}, \mathbf{A} \mid \mathbf{y}) \propto p(\boldsymbol{\theta}, \boldsymbol{\beta}, \tau_s, \mathbf{V}, \boldsymbol{\gamma}, \boldsymbol{\rho}, \boldsymbol{\eta}, \mathbf{A}) \times \prod_{i=1}^n \prod_{d=1}^q p(y_{id} \mid \phi_{id}),$$

where $\mathbf{y} = (\mathbf{y}_1^T, \dots, \mathbf{y}_q^T)^T$ is $N \times 1$ with $N = nq$, n is the number of geographic regions, and $\mathbf{y}_d = (y_{1d}, \dots, y_{nd})^T$ and each y_{id} being modeled independently conditional on the spatial random effects using a member from the exponential family. For example, in our subsequent analysis we assume $y_{id} \mid \boldsymbol{\beta}_d, \phi_{id} \stackrel{ind}{\sim} Pois(E_{id} \exp(\mathbf{x}_{id}^T \boldsymbol{\beta}_d + \phi_{id}))$ and specify the joint prior distribution, $p(\boldsymbol{\theta}, \boldsymbol{\beta}, \tau_s, \mathbf{V}, \boldsymbol{\gamma}, \boldsymbol{\rho}, \boldsymbol{\eta}, \mathbf{A})$ proportional to

$$(12) \quad \prod_{d=1}^q \mathcal{N}(\boldsymbol{\beta}_d \mid \mathbf{0}, \boldsymbol{\Sigma}_{\beta_d}) \times \prod_{k=1}^K \{\mathcal{N}(\theta_k \mid 0, 1/\tau_s) \times Beta(V_k \mid 1, \alpha)\} \\ \times IG(1/\tau_s \mid a_s, b_s) \times \mathcal{N}(\boldsymbol{\gamma} \mid \mathbf{0}, \boldsymbol{\Sigma}_\gamma) \times \mathcal{W}^{-1}(\mathbf{A}\mathbf{A}^T \mid \nu, \boldsymbol{\Psi}) \times \left| \frac{\partial \mathbf{A}\mathbf{A}^T}{\partial a_{dh}} \right| \\ \times \prod_{d=1}^q \left\{ \prod_{r=1}^{R_d} \mathcal{U}(\eta_{dr} \mid 0, M_r) \times \mathcal{U}(\rho_d \mid 0, 1) \right\},$$

where $\left| \frac{\partial \mathbf{A}\mathbf{A}^T}{\partial a_{dh}} \right| = 2^q \prod_{d=1}^q a_{dd}^{q-d+1}$ is the Jacobian transformation for the prior on $\mathbf{A}\mathbf{A}^T$ in terms of the Cholesky factor \mathbf{A} (Olkin and Sampson, 1972), and R_d is the dimension of $\boldsymbol{\eta}_d$. We employ Markov Chain Monte Carlo (MCMC) with Gibbs sampling and random walk Metropolis (Gamerman and Lopes, 2006), implemented in R statistical computing environment, to draw samples from the posterior distribution, as defined in (11).

The graphical models discussed above provide parametric representations for \mathbf{A} . Therefore, the $\mathcal{W}(\mathbf{A}\mathbf{A}^T \mid \cdot, \cdot)$ in (12) is replaced with priors on the parameters defining \mathbf{A} . In the directed graphical setting, we further model $\mathbf{A}_{d,h}$ in terms of parameters $\{\alpha_{0dd'}\}$ and $\alpha_{1dd'}$. These parameters are all assigned independent Gaussian prior distributions $\alpha_{0dd'} \stackrel{ind}{\sim} \mathcal{N}(\cdot, \cdot)$ and $\alpha_{1dd'} \stackrel{ind}{\sim} \mathcal{N}(\cdot, \cdot)$, respectively, resulting in a joint prior distribution for the whole $\boldsymbol{\alpha} = (\alpha_{0dd'}, \alpha_{1dd'})_{d,d'}$ vector parameter, i.e., $\boldsymbol{\alpha} \sim \mathcal{N}(\mathbf{0}, 100\mathbf{I})$. In the undirected model, the unknown parameter is ρ_{dis} which specifies \mathbf{A} completely so we model $\rho_{dis} \stackrel{ind}{\sim} \mathcal{U}(\cdot, \cdot)$. Details on the computations are presented in Appendix A.

3.5. *Difference boundaries through FDR.* We treat spatial boundary analysis as an exercise in multiple hypothesis testing, although a formal null hypothesis is not required in Bayesian inference. Instead, we pursue full stochastic quantification to derive a threshold for detecting cancer-specific spatial disparities. For each pair of adjacent regions, i.e., $i \sim j$, and each cancer d , we seek the posterior probability of $\phi_{id} = \phi_{jd}$ and its complement $\phi_{id} \neq \phi_{jd}$ for region-disease pairs (i, d) and (j, d') . We designate edge (i, j) as a difference boundary if the posterior probability of $\phi_{id} \neq \phi_{jd}$ given \mathbf{y} surpasses a predefined threshold t .

The most general difference boundary we report is the *cross-difference* boundary based upon $v_{(i,d)(j,d')} = P(\phi_{id} \neq \phi_{jd'}, \phi_{id'} \neq \phi_{jd} \mid \mathbf{y})$. We derive a threshold t that controls the false

discovery rate (FDR) below a level $\zeta = 0.05$. To this end, we define

$$(13) \quad \text{FDR}_{d,d'}(t) = \frac{\sum_{i \sim j} I(\phi_{id} = \phi_{jd'}) I(v_{(i,d)(j,d')} > t)}{\sum_{i \sim j} I(v_{(i,d)(j,d')} > t)}$$

every disease pair d and d' . The quantity in (13) is evaluated as

$$(14) \quad \widehat{\text{FDR}}_{d,d'}(t) = \mathbb{E}[\text{FDR}_{d,d'} | \mathbf{y}] = \frac{\sum_{i \sim j} (1 - v_{(i,d)(j,d')}) I(v_{(i,d)(j,d')} > t)}{\sum_{i \sim j} I(v_{(i,d)(j,d')} > t)}.$$

Following Müller et al. (2004), we define

$$(15) \quad t^* = \sup \left\{ t : \widehat{\text{FDR}}_{d,d'}(t) \leq \zeta \right\},$$

which is based upon the optimal decision that minimizes the estimated false negative rate (FNR), $\widehat{\text{FNR}}_{d,d'}(t) = \frac{\sum_{i \sim j} v_{(i,d)(j,d')} (1 - I(v_{(i,d)(j,d')} > t))}{m - \sum_{i \sim j} I(v_{(i,d)(j,d')} > t)}$, where m is the total number of geographic boundaries, subject to $\widehat{\text{FDR}} \leq \zeta$ (also see Sun et al., 2015, who proffer a similar approach). This estimation is based on a bivariate loss function $L_{2R} = (\widehat{\text{FDR}}, \widehat{\text{FNR}})$.

Note that the case of a single disease arises by substituting $v_{i,j}^{(d)} = P(\phi_{id} \neq \phi_{jd}, \phi_{id} \neq \phi_{jd} | \mathbf{y})$ in the above expressions. This is analogous to the formulation in Li et al. (2015) but with the added flexibility of modeling the adjacency matrices and taking into account more detailed disease dependency structures.

4. Simulation experiments. We generated count data for $q = 4$ diseases using (1) assuming $y_{id} \stackrel{\text{ind}}{\sim} \text{Pois}(\exp(\beta_d + \phi_{id}))$ over the $N = 58$ counties in California. The counts were generated after simulating spatial effects $\phi = (\phi_1^T, \phi_2^T, \phi_3^T, \phi_4^T)^T \sim G_N$ with parameters fixed as $K = 15$, $\alpha = 1$, $\beta_1 = -2$, $\beta_2 = 2$, $\beta_3 = 1$, $\beta_4 = -1$, and $\tau_s = 0.25$. We present simulations under three different settings corresponding to the 3 graphs in Figure 4: (i) unstructured; (ii) directed; and (iii) undirected. These imply 3 different specifications for Σ_γ in $\gamma \sim \mathcal{N}(\mathbf{0}, \Sigma_\gamma)$. For each of these settings we generate 25 data sets by fixing all parameters required to specify the underlying distributions as described below.

For each of the above models, Σ_γ depends upon the DAGAR parameters and the inter-disease covariances. Spatial correlation parameters for the different cancers are fixed as $\rho = (0.2, 0.8, 0.4, 0.6)^T$. For the adjacency matrices, \mathbf{W}_d , the elements z_{ij} of the \mathbf{Z} matrix are computed as the standardized absolute difference of a generated covariate $|x_i - x_j|/\sigma$. We generate each x_i from a normal distribution with mean 15 and standard deviation 5, while σ represents the standard deviation of all the absolute differences between the x_i values across all pairs of contiguous areas. The unknown parameters associated with these variables were fixed at $\boldsymbol{\eta} = (0.5, 0.25, 0.33, 0.6)^T$. In addition to specifying the DAGAR parameters for each disease, for (i) we specify \mathbf{A} as lower triangular with all elements set to 1. For (ii) we fix $(\alpha_{021}, \alpha_{121})^T = (0.3, 0.5)^T$, $(\alpha_{041}, \alpha_{141})^T = (0.5, 0.4)^T$, $(\alpha_{032}, \alpha_{132})^T = (0.4, 0.4)^T$, and $(\alpha_{043}, \alpha_{143})^T = (0.8, 0.1)^T$, and for (iii) we fix $\rho_{dis} = 0.25$. For each of these scenarios, we produce a single instance of Σ_γ , which is used to generate a corresponding instance of γ . This yields one set of spatial random effects which are retained in generating the counts for the 25 data sets. Figure 5 illustrates the maps of random effects for the four diseases in the generated data using the unstructured disease graph. A total of six distinct levels are observed with values ranging from -5.51 to 2.37 arranged in ascending order. There are 99 “true difference boundaries” for disease 1, 83 for disease 2, 91 for disease 3 and 89 for disease 4. The Appendix presents additional maps for data generated using the directed (Figure 22) and undirected (Figure 23) disease graphs.

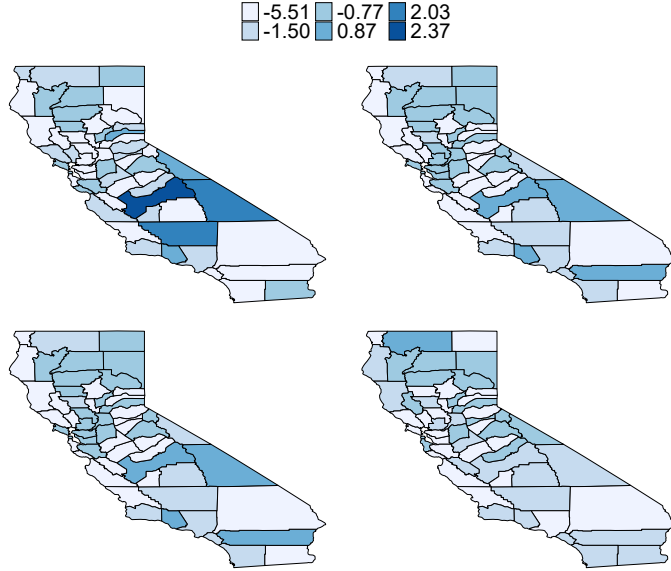


Fig 5: Simulated data maps depicting the random effects for the four cancers using a disease unstructured graph.

We apply our model to the 25 simulated data sets generated as described above. For the data analysis, we specify the prior hyperparameters as $\sigma_{\beta_0}^2 = 1$, $a_s = 2$, $b_s = 1$, $\alpha = 1$, and $M = -\log(0.5)/\mathbf{Z}_{0.5}$, where $\mathbf{Z}_{0.5}$ represents the 0.5th quantile of the \mathbf{Z} matrix. For the unstructured or unconstrained inter-disease graph (left panel in Figure 4) we use the Wishart distribution in (12) with $\nu = 2$ and $\Psi = \text{diag}(0.1, 0.1, 0.1, 0.1)$. For the directed graph (center panel in Figure 4), \mathbf{A} is determined through $\alpha \sim \mathcal{N}(\mathbf{0}, 100\mathbf{I})$, while for the undirected graph (right panel in Figure 4) we specify $\rho_{dis} \sim \mathcal{U}(-1, 1)$. We perform boundary detection by computing the conditional probability, $P(\phi_{id} \neq \phi_{jd'} | \mathbf{y})$, for d and d' ranging from 1 to 4, across neighboring regions denoted as i and j . We use these posterior probabilities to obtain boundary detection results in terms of sensitivity and specificity for all pairs of regions and for all the disease graph models.

For each data set, we present inference based on 2,500 posterior samples using Markov Chain Monte Carlo (MCMC) algorithms after discarding the initial 2,500 iterations as burn-in. Table 1 presents the corresponding results. For each simulation, the values of sensitivity and specificity are determined by selecting a fixed number of edges with the highest T posterior probabilities, where $T \in \{80, 90, 100, 110, 120\}$. This selection accounts for false positives in all other T values for the diseases. The values in Table 1 are average values of sensitivity and specificity over the 25 simulated data sets.

In considering the true boundaries specified above and selecting 110 boundaries from posterior computations, sensitivities of approximately 80% are achieved for all diseases except the second one, which surpasses 90%. This may appear somewhat subdued in comparison to results from Gao, Banerjee and Ritz (2022), but is not entirely unexpected. In fact, these lower values are a consequence of introducing the uncertainty in the adjacency matrix. This additional uncertainty, imposed on the adjacency structure, propagates through the model resulting in a significantly wider posterior distribution for spatial random effects. A broader posterior distribution signifies an increased occurrence of ties between random effects across various cancers and regions. Consequently, a greater number of ties produces fewer difference boundaries, which, in turn, yield lower sensitivity values. Conversely, when more boundaries

TABLE 1
Boundary detection results in the simulation study for the three disease graph models.

Disease graph	T	Disease 1		Disease 2		Disease 3		Disease 4	
		Specificity	Sensitivity	Specificity	Sensitivity	Specificity	Sensitivity	Specificity	Sensitivity
Unstructured	80	0.470	0.596	0.729	0.790	0.503	0.602	0.432	0.582
	90	0.395	0.665	0.630	0.839	0.405	0.665	0.367	0.656
	100	0.302	0.729	0.519	0.881	0.319	0.734	0.293	0.727
	110	0.239	0.804	0.395	0.918	0.231	0.799	0.208	0.791
	120	0.144	0.867	0.263	0.949	0.145	0.866	0.131	0.861
Directed	80	0.433	0.619	0.621	0.821	0.459	0.600	0.427	0.578
	90	0.358	0.678	0.532	0.870	0.383	0.668	0.358	0.651
	100	0.298	0.749	0.435	0.912	0.304	0.737	0.287	0.724
	110	0.215	0.808	0.315	0.943	0.233	0.809	0.214	0.795
	120	0.142	0.875	0.215	0.973	0.152	0.874	0.135	0.863
Undirected	80	0.458	0.595	0.588	0.898	0.385	0.563	0.411	0.568
	90	0.377	0.661	0.497	0.929	0.316	0.638	0.340	0.642
	100	0.301	0.730	0.396	0.946	0.238	0.721	0.263	0.711
	110	0.220	0.799	0.293	0.958	0.185	0.795	0.182	0.777
	120	0.139	0.873	0.193	0.976	0.124	0.868	0.115	0.851

TABLE 2
Adjacencies detection for the three disease graph models.

Disease graph	Disease 1		Disease 2		Disease 3		Disease 4	
	Specificity	Sensitivity	Specificity	Sensitivity	Specificity	Sensitivity	Specificity	Sensitivity
Unstructured	0.373	1.000	0.878	0.912	0.692	0.981	0.384	1.000
Directed	0.431	0.999	0.720	0.926	0.743	0.976	0.412	1.000
Undirected	0.456	0.995	0.562	0.952	0.597	0.962	0.304	1.000

are detected, the specificity is consequently reduced. Table 1 also presents the results concerning the directed and undirected disease graphs, where similar considerations apply. Table 4 in the Appendix presents the values of specificity and sensitivity for the three cancer disease graph choices cross-cancer boundary detection. Also in this case analogous aspects and considerations to those presented here are drawn.

Regarding the adjacency model, Table 2 reports values of specificity and sensitivity regarding the detection of boundaries. Apparently, higher values of sensitivity are obtained for all the diseases and for all the disease graph models, while specificity values are smaller. High sensitivity and low specificity imply that our model is sensitive to detecting true positives, but may also misidentify some negative cases as positive (false positives). While false positives are undesirable, this does not represent a major issue for our application in spatial health disparities where policy is dictated by true positives.

Figure 6 presents the distributions of WAIC values (Watanabe and Opper, 2010), a generalized version of the Akaike information criterion, across multiple simulations for the three disease graphs. This metric gauges the extent of information loss in a given model, the less the better, by effectively addressing the risks of both overfitting and underfitting. Notably, in terms of WAIC values, the directed graph stands out with superior performance, while the other two graphs exhibit closely aligned values. This close resemblance might stem from the fact that the unstructured and undirected graphs bear similarity in interpretation; the former is essentially analogous to an undirected graph where all nodes are interconnected.

5. SEER cancers analysis. We analyze the data set described in Section 2 using a Poisson spatial regression model. Specifically, we model the observed counts of incidence, for each county and for each cancer, as $y_{id} | \beta_d, \phi_{id} \stackrel{ind}{\sim} Pois(E_{id} \exp(\mathbf{x}_{id}^T \beta_d + \phi_{id}))$ for

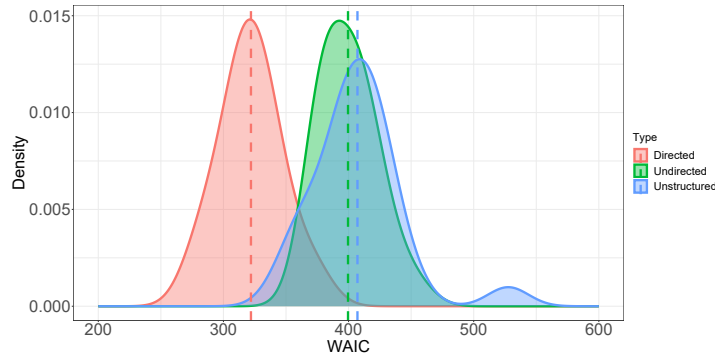


Fig 6: WAIC comparison for different choices of the disease graph.

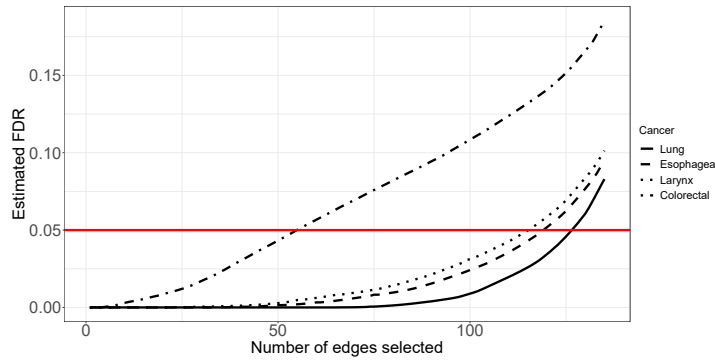


Fig 7: Estimated FDR curves plotted against the number of selected difference boundaries for four cancers

$i = 1, \dots, 58$ and $d = 1, \dots, 4$. Following the prior specification outlined in the simulation study, we employ the model discussed in Section 3 to represent γ with adjacency modeling within the MDAGAR model and unstructured disease graph. Here, we draw diagnostic inference based upon 10,000 posterior samples using MCMC algorithms after discarding an initial 20,000 iterations as burn-in. Throughout this Section, it is worth noting, we comment on the results by directly referring to specific counties by their names. For a visual reference of the corresponding county names, we refer the reader to the Appendix and the map there depicted in Figure 12.

We employ a threshold to control for FDR as specified in (15) for detecting difference boundaries for each cancer. Figure 7 illustrates the change in estimated FDR with different numbers of selected edges as differential boundaries for the four cancers individually using adjacency modeling within MDAGAR. We observed analogous FDR curves for lung, esophageal and larynx cancer leading us to select a similar number of boundaries for these three cancers with a threshold of $\zeta = 0.05$. Conversely, we detect a smaller number of boundaries for colorectal cancer using the same threshold.

Setting $\zeta = 0.05$ in (15), Figure 8 illustrates the identified difference boundaries (highlighted in red) in the SIR maps for the four types of cancers. The width of the lines on the boundaries signify higher probabilities of detection. Notably, lung cancer exhibits the highest number of detected boundaries, i.e., 126, with esophageal and larynx cancers demonstrating a much higher number of boundaries, i.e., 119 and 115, compared to colorectal cancer with 54 boundaries. It is worth noting that the detected boundaries for the various cancers tend to form geographical clusters, which bring together regions with similar random effects.

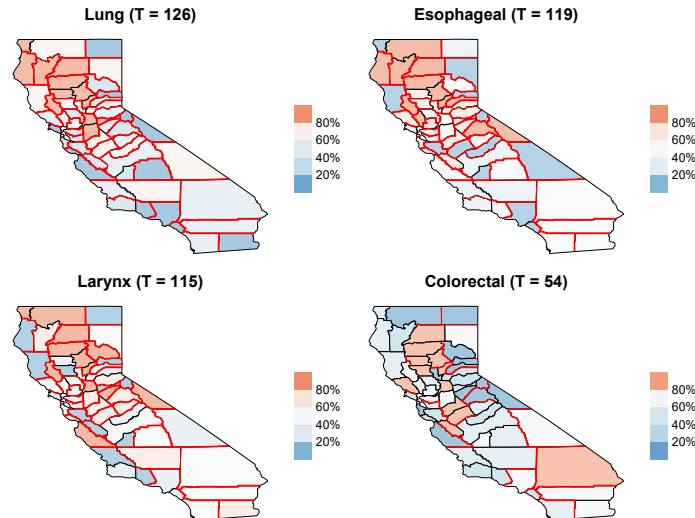


Fig 8: Difference boundaries (highlighted in red) detected by the model in SIR map for four cancers individually when $\zeta = 0.05$. The values in brackets are the number of difference boundaries detected.

For instance, in northern California, we observe clustering of certain regions (Tehama, Glenn, Butte, and Yuba) with a high lung SIR value. These regions also exhibit similar patterns for esophageal and larynx cancers indicating spatial association. This is evident from the maps depicting shared difference and mutual cross-difference boundaries in Figure 9, where these regions display identical random effects. Such consistency is likely attributable to the strong correlation among these cancers. A similar pattern is observed in the central regions, namely Solano, Sacramento, and San Joaquin, with lung SIR values ranging from 60% to 100%. The esophageal and larynx cancer maps also exhibit comparable dynamics. However, identifying spatial patterns for colorectal cancer is more challenging. These disparities are likely due to our accounting for smoking standardized differences in both the adjacency and mean models. It is well-known that smoking has a significant influence, particularly on the development of lung, esophageal, and larynx cancers (Doll et al., 2005).

For distinguishing boundaries among cancers, we examine both shared difference boundaries and mutual cross-cancer boundaries. The shared difference boundaries refer to the boundaries detected in common across different cancers. Figure 9 illustrates the shared boundaries for each cancer pair, denoted as $P(\phi_{id} \neq \phi_{jd}, \phi_{id'} \neq \phi_{jd'} | \mathbf{y})$ where $d \neq d'$. We have observed consistent detection of specific boundaries whenever the lung is affected, including Siskiyou-Modoc, Siskiyou-Shasta, Nevada-Placer and Santa Clara-Stanislaus. Similarly, when examining all cancers, similar patterns emerge in Los Angeles county. Notably, the Los Angeles-San Bernardino border, as well as Orange-San Bernardino, Orange-Riverside and Riverside-San Diego, are consistently identified.

We introduce a mutual cross-cancer boundary denoted by $P(\phi_{id} \neq \phi_{jd'}, \phi_{id'} \neq \phi_{jd} | \mathbf{y})$, where $i \sim j$ and $i < j$, to ascertain boundaries for cross-cancer differences. This boundary effectively segregates the effects pertaining to distinct cancers across adjacent counties (see Figure 10). Upon analysis, we observe distinct variations between counties in terms of lung-esophageal and lung-larynx differences. It is evident that the number of detected borders is significantly higher for lung-esophageal, lung-larynx and esophageal-larynx cancers compared to other types. Moreover, when considering these three cases, Orange County demonstrates clear separation from Riverside and San Diego counties, indicating notable differences in their respective lung-related conditions.

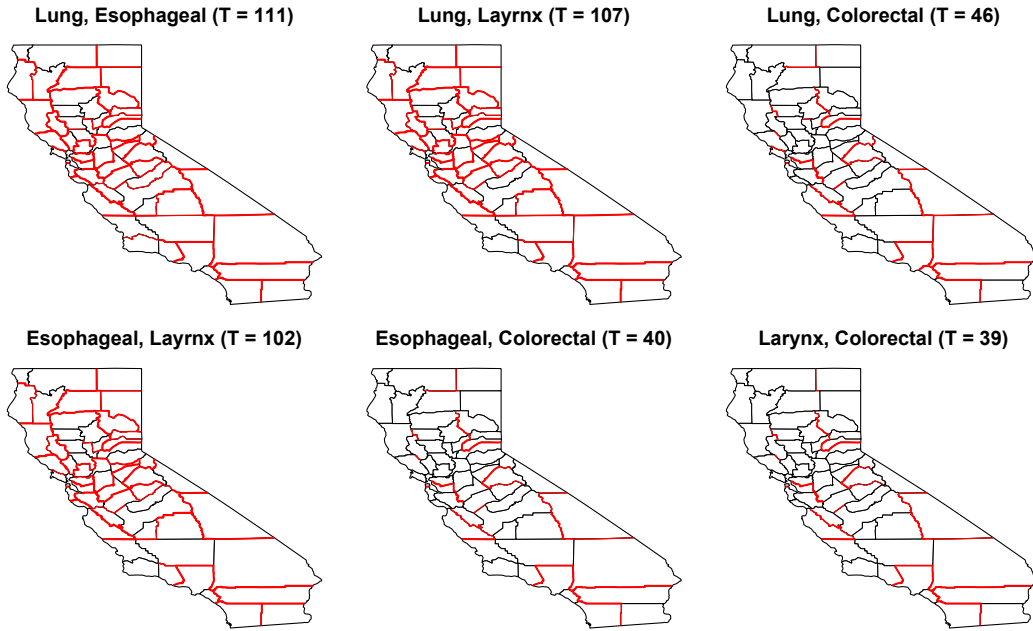


Fig 9: Shared difference boundaries (highlighted in red) detected by the model for each pair of cancers in SIR map when $\zeta = 0.05$. The values in brackets are the number of difference boundaries detected.

Including explanatory variables affect difference boundary detection, leading to either larger or smaller numbers of such boundaries. For instance, a covariate intensifies the contrast in residual spatial effects between two adjacent counties, a difference boundary is more likely to be observed between them. Conversely, if a covariate reduces the disparity in residual spatial effects between neighboring counties, the presence of a difference boundary may diminish. The former occurs, for example, for lung, esophageal and larynx boundary detection individually, while the latter is probably seen for colorectal for which we detect fewer boundaries. The impact of covariates on the number of difference boundaries depends on how they affect the variation in rates across neighboring counties. It is important to note that while covariates always absorb some spatial effects, the relationships among cancers, regions, and covariates are intricate, and a definitive pattern is not always discernible.

Turning to adjacency modeling, in the following we will say that a non-adjacency is detected based on the following probabilities:

$$(16) \quad P(w_{d,ij} = 0 \mid \mathbf{y}, i \sim j)$$

where $w_{d,ij}$ represents the (i, j) -th element of the adjacency matrix corresponding to the d -th cancer. Figure 11 depicts a map of California with these probabilities represented by the thickness of the boundaries. As is evident in Figure 11, the majority of the borders are not colored in blue. This absence of blue indicates that the probability of $w_{d,ij}$ being 0 is null, implying that adjacency detection is performed for those geographic boundaries. Considering all the cancers under investigation, the detected non-adjacencies are 32 for lung, 12 for esophageal, 31 for larynx and 29 for colorectal. These correspond, respectively, to approximately 23%, 9%, 22% and 21% of the total number of borders.

In general, it is evident that the detected non-adjacencies predominantly occur in counties with high smoking rates. Conversely, counties with lower smoking rates consistently exhibit zero detected non-adjacencies. This pattern strongly suggests that smoking serves as

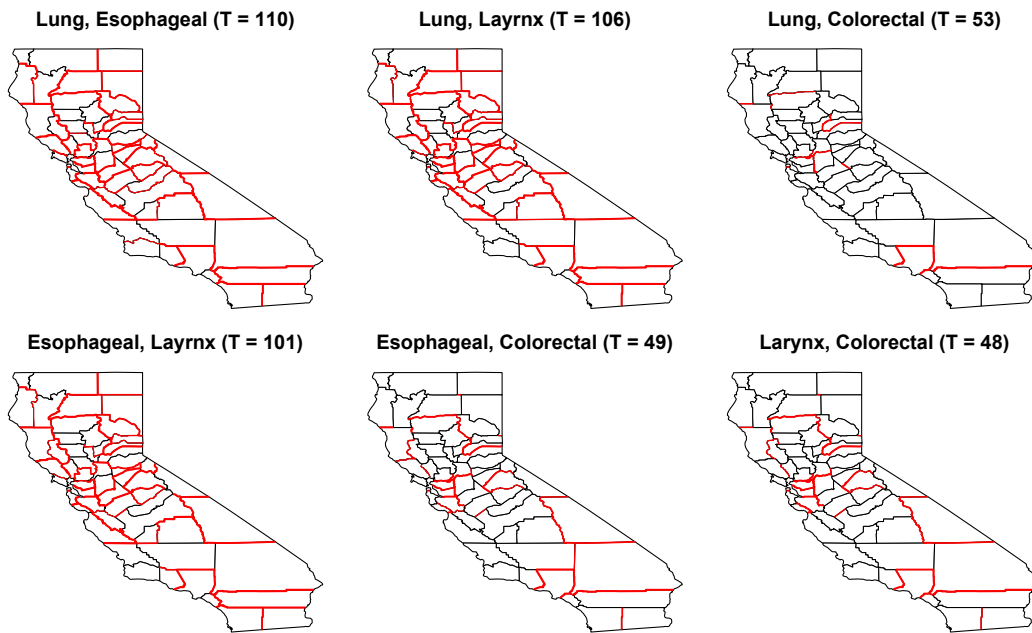


Fig 10: Mutual cross-difference boundaries (highlighted in red) detected by the model for each pair of cancers in SIR map when $\zeta = 0.05$. The values in brackets are the number of difference boundaries detected.

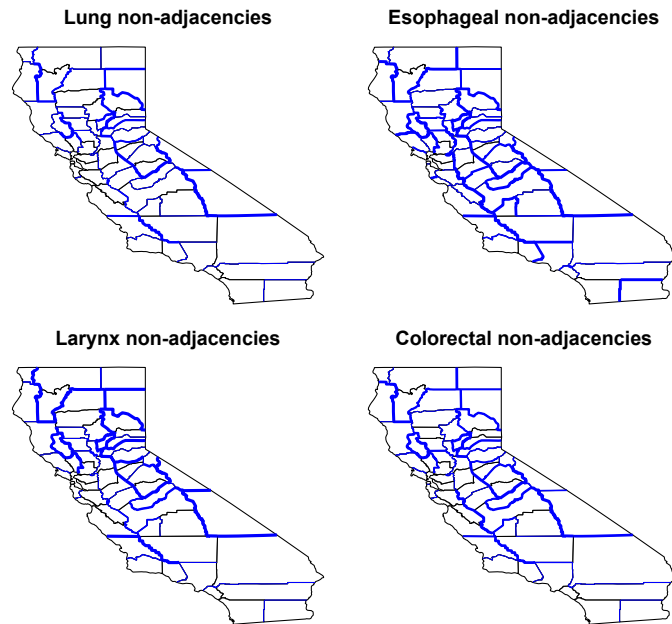


Fig 11: Non-adjacencies (shown in blue) overlaid on smoking rates. The thickness of the lines is proportional to the probability of being considered as a non-adjacency

a suitable dissimilarity metric for identifying these boundaries, as the estimated boundaries closely align with significant variations in the smoking covariate. However, it is worth noting that a few of the identified boundaries do not show evidence of separating areas with dif-

fering smoking rates. Examples of such boundaries include Trinity-Shasta, Siskiyou-Shasta, Trinity-Tehama, Lake-Colusa, and Lake-Glenn. These cases indicate that factors other than smoking may contribute to the observed differences in cancer occurrence or that the boundaries in these particular instances are not solely determined by smoking rates. This occurrence may be attributed to the significant variations in cancer counts between the counties, as the values can differ greatly. Therefore, the presence or absence of detected non-adjacencies in these cases may be influenced by factors other than smoking rates alone.

Through our comprehensive analysis, we discover that there exists a strong correlation among lung, esophageal, and larynx cancers. The findings of this study highlight the interconnected nature of these specific types of cancers, suggesting common risk factors or underlying mechanisms that contribute to their occurrence. A compelling aspect of this association is revealed through the visual representations of the three maps we have presented. These maps vividly illustrate remarkably similar spatial clusters for lung, esophageal, and larynx cancers. The clustering patterns observed strongly imply that the corresponding random effects associated with these cancers share identical values. This consistency in spatial distribution reinforces the notion that these cancers are closely related and potentially influenced by shared factors. The spatial clusters observed in these maps indicate that the incidence and prevalence of lung, esophageal, and larynx cancers tend to occur in close proximity to one another. This spatial pattern may be influenced by a multitude of factors, including geographical characteristics, socioeconomic factors, or specific cultural and lifestyle factors prevalent in certain regions. Understanding the spatial relationships can provide valuable insights into the complex interplay between environmental and individual risk factors.

In the Appendix two distinct settings of the model are presented for this study. The first setting involves incorporating covariates solely in the adjacency model, while the second setting integrates covariates exclusively in the mean structure while maintaining fixed adjacencies. These additional maps provide valuable insights into the impact of covariates on the overall analysis. By examining the effects of covariates within the adjacency model, we gain a better understanding of how specific factors contribute to the spatial patterns observed in the data. Similarly, the inclusion of covariates solely in the mean structure, with fixed adjacencies, allows us to investigate the influence of these variables on the overall mean values of the observed phenomena.

6. Discussion. The developments in this manuscript address statistical methods for detecting spatial health disparities based upon mapping disease rates and modeling difference boundaries. The need for formal modeling in ascertaining health disparities has been articulated in the literature (see, e.g., [Rao, 2023](#), and references therein), but formal model based approaches for detecting geographic disparities remain relatively scarce. The inferential framework developed here achieves full probabilistic uncertainty quantification. The idea is to use a flexible (nonparametric) prior on the spatial effects that will endow discrete masses to spatial random effects to detect discrepancies among neighbors while also allowing spatial smoothing across neighbors as is customary in disease mapping.

Our methodology extends some recent work by [Gao, Banerjee and Ritz \(2022\)](#) in multiple directions. As there, we also deal with multiple diseases, possibly associated among themselves, but now explicitly address multivariate dependencies more flexibly using posited graphical models. Second, we address a possible limitation of [Gao, Banerjee and Ritz \(2022\)](#) where factors directly influencing difference boundaries need to be evaluated using their inclusion and exclusion in models with subsequent model assessment. Instead, we introduce the possible incorporation of such factors in the adjacency modeling to evaluate its effects. This enriches earlier statistical frameworks for “areal wombling” that have attempted similar adjacency models with limited effectiveness since statistical significance of boundary effects is

difficult to establish with such hierarchically embedded information. Our framework, on the other hand, allows flexible modeling of boundaries (as in “wombling”), but uses a Bayesian FDR approach to ascertain spatial difference boundaries.

Our application to the SEER database leads to data-based discoveries with regard to the impact of associations among cancers in detecting spatial disparities. The high correlation among lung, esophageal, and larynx cancers carries significant implications for public health initiatives and cancer prevention strategies. The associations among these cancers suggest that interventions targeting one of these malignancies could potentially have a positive impact on reducing the incidence and burden of the others. By recognizing the shared patterns and risk factors, healthcare professionals and policymakers can develop more targeted and effective interventions. In response to these findings, a multifaceted approach should be employed to address this correlation and reduce the overall burden of these cancers. This approach should encompass public awareness campaigns to educate individuals about the shared risk factors and promote healthy lifestyle choices.

SUPPLEMENTARY MATERIAL

Supplementary material is provided in the Appendix. It includes the sampling scheme, consideration on Monte Carlo standard errors, the map with the county names, maps regarding different model settings for the data analysis, additional plots and tables for the simulation. Computer programs to reproduce the numerical experiments and data analyses are available at <https://github.com/lucaaiello/graphical-models-for-boundary-detection/tree/main>

REFERENCES

- AGRAWAL, K., MARKERT, R. J. and AGRAWAL, S. (2018). Risk factors for adenocarcinoma and squamous cell carcinoma of the esophagus and lung. *Hypertension* **61** 0–09. [3](#)
- AKHTAR, J., BHARGAVA, R., SHAMEEM, M., SINGH, S. K., BANEEN, U., KHAN, N. A., HASSAN, J. and SHARMA, P. (2010). Second primary lung cancer with glottic laryngeal cancer as index tumor—A case report. *Case reports in oncology* **3** 35–39. [3](#)
- BANERJEE, S. (2016). Multivariate spatial models. In *Handbook of Spatial Epidemiology* (A. B. Lawson, S. Banerjee, R. P. Haining and M. D. Ugarte, eds.) 375–397. Taylor & Francis/CRC Press, Boca Raton, FL. [9](#)
- BANERJEE, S., CARLIN, B. P. and GELFAND, A. E. (2014). *Hierarchical Modeling And Analysis For Spatial Data*. CRC press. [4](#), [10](#)
- CARLIN, B. P. and BANERJEE, S. (2003). Hierarchical Multivariate CAR Models for Spatio-temporally Correlated Survival Data. *Bayesian Statistics* **7** 45–63. [9](#), [10](#)
- CORPAS-BURGOS, F. and MARTINEZ-BENEITO, M. A. (2020). On the use of adaptive spatial weight matrices from disease mapping multivariate analyses. *Stochastic Environmental Research and Risk Assessment* **34** 531–544. [1](#), [2](#)
- COX, D. R. and WERMUTH, N. (1993). Linear Dependencies Represented by Chain Graphs. *Statistical Science* **8** 204 – 218. [9](#)
- COX, D. R. and WERMUTH, N. (1996). *Multivariate Dependencies*. Chapman & Hall/CRC, Boca Raton, FL. [9](#)
- DATTA, A., BANERJEE, S., HODGES, J. S. and GAO, L. (2019). Spatial disease mapping using directed acyclic graph auto-regressive (DAGAR) models. *Bayesian analysis* **14** 1221. [2](#), [7](#), [9](#)
- DOLL, R., PETO, R., BOREHAM, J. and SUTHERLAND, I. (2005). Mortality from cancer in relation to smoking: 50 years observations on British doctors. *British journal of cancer* **92** 426–429. [4](#), [16](#)
- FITZPATRICK, M. C., PREISSER, E. L., PORTER, A., ELKINTON, J., WALLER, L. A., CARLIN, B. P. and ELLISON, A. M. (2010). Ecological boundary detection using Bayesian areal wombling. *Ecology* **91** 3448–3455. [1](#)
- FLEGAL, J. M., HUGHES, J., VATS, D., DAI, N., GUPTA, K. and MAJI, U. (2021). mcmcse: Monte Carlo Standard Errors for MCMC, Riverside, CA, and Kanpur, India R package version 1.5-0. [24](#)
- GAMERMAN, D. and LOPES, H. F. (2006). *Markov chain Monte Carlo: stochastic simulation for Bayesian inference*. CRC press. [11](#), [22](#)
- GAO, L., BANERJEE, S. and RITZ, B. (2022). Spatial difference boundary detection for multiple outcomes using Bayesian disease mapping. *Biostatistics*. [1](#), [2](#), [5](#), [7](#), [9](#), [13](#), [19](#)

- GAO, L., DATTA, A. and BANERJEE, S. (2022). Hierarchical multivariate directed acyclic graph autoregressive models for spatial diseases mapping. *Statistics in Medicine* **41** 3057–3075. [9](#)
- GELFAND, A. E. and VOUNATSOU, P. (2003). Proper Multivariate Conditional Autoregressive Models for Spatial Data Analysis. *Biostatistics* **4** 11–15. [9](#), [10](#)
- GONG, L. and FLEGAL, J. M. (2016). A practical sequential stopping rule for high-dimensional Markov chain Monte Carlo. *Journal of Computational and Graphical Statistics* **25** 684–700. [24](#)
- HANSON, T., BANERJEE, S., LI, P. and MCBEAN, A. (2015). Spatial Boundary Detection for Areal Counts. In *Nonparametric Bayesian Inference in Biostatistics* 377–399. Springer. [1](#)
- NATIONAL CANCER INSTITUTE (2019). SEER*Stat Software. [3](#)
- JACQUEZ, G. M. and GREILING, D. A. (2003a). Local Clustering in Breast, Lung and Colorectal Cancer in Long Island, New York. *International Journal of Health Geographics* **2** 1–12. [1](#)
- JACQUEZ, G. M. and GREILING, D. A. (2003b). Geographic Boundaries in Breast, Lung and Colorectal Cancers in Relation to Exposure to Air Toxics in Long Island, New York. *International Journal of Health Geographics* **2** 1–22. [1](#)
- JIN, X., BANERJEE, S. and CARLIN, B. P. (2007). Order-free co-regionalized areal data models with application to multiple-disease mapping. *Journal of the Royal Statistical Society: Series B (Statistical Methodology)* **69** 817–838. [9](#)
- JIN, X., CARLIN, B. P. and BANERJEE, S. (2005). Generalized hierarchical multivariate CAR models for areal data. *Biometrics* **61** 950–961. [3](#), [9](#)
- KALLI, M., GRIFFIN, J. E. and WALKER, S. G. (2011). Slice sampling mixture models. *Statistics and computing* **21** 93–105. [6](#)
- KOCH, T. (2005). *Cartographies of disease: maps, mapping, and medicine*. Esri Press Redlands, CA. [1](#)
- KURISHIMA, K., MIYAZAKI, K., WATANABE, H., SHIOZAWA, T., ISHIKAWA, H., SATOH, H. and HIZAWA, N. (2018). Lung cancer patients with synchronous colon cancer. *Molecular and clinical oncology* **8** 137–140. [3](#)
- LAWSON, A. B. (2013). *Statistical methods in spatial epidemiology*. John Wiley & Sons. [1](#)
- LAWSON, B. ANDREW, BANERJEE, S., HAINING, R. and UGARTE, D. MARIA (2016). *Handbook of Spatial Epidemiology*. CRC press, Boca Raton, FL. [1](#)
- LEE, D. and MITCHELL, R. (2012). Boundary detection in disease mapping studies. *Biostatistics* **13** 415–426. [2](#), [7](#), [8](#)
- LI, P., BANERJEE, S. and MCBEAN, A. M. (2011). Mining boundary effects in areally referenced spatial data using the Bayesian information criterion. *Geoinformatica* **15** 435–454. [1](#), [8](#)
- LI, P., BANERJEE, S., CARLIN, B. P. and MCBEAN, A. M. (2012). Bayesian Areal Wombling Using False Discovery Rates. *Statistics and its Interface* **5** 149–158. [1](#), [2](#)
- LI, P., BANERJEE, S., HANSON, T. A. and MCBEAN, A. M. (2015). Bayesian models for detecting difference boundaries in areal data. *Statistica Sinica* **25** 385. [1](#), [2](#), [12](#)
- LU, H. and CARLIN, B. P. (2005). Bayesian Areal Wombling for Geographical Boundary Analysis. *Geographical Analysis* **37** 265–285. [1](#)
- LU, H., REILLY, C. S., BANERJEE, S. and CARLIN, B. P. (2007). Bayesian areal wombling via adjacency modeling. *Environmental and ecological statistics* **14** 433–452. [1](#), [2](#), [7](#)
- MA, H. and CARLIN, B. P. (2007). Bayesian Multivariate Areal Wombling for Multiple Disease Boundary Analysis. *Bayesian Analysis* **2** 281–302. [1](#)
- MA, H., CARLIN, B. P. and BANERJEE, S. (2010). Hierarchical and joint site-edge methods for Medicare hospice service region boundary analysis. *Biometrics* **66** 355–364. [1](#), [2](#), [8](#)
- MACNAB, Y. C. (2018). Some recent work on multivariate Gaussian Markov random fields (with discussion). *TEST: An Official Journal of the Spanish Society of Statistics and Operations Research* **27** 497–541. [9](#)
- MARDIA, K. (1988). Multi-dimensional multivariate Gaussian Markov random fields with application to image processing. *Journal of Multivariate Analysis* **24** 265–284. [9](#), [10](#)
- MIASOJEDOW, B., MOULINES, E. and VIHOLA, M. (2013). An adaptive parallel tempering algorithm. *Journal of Computational and Graphical Statistics* **22** 649–664. [22](#)
- MÜLLER, P., PARMIGIANI, G., ROBERT, C. and ROUSSEAU, J. (2004). Optimal sample size for multiple testing: the case of gene expression microarrays. *Journal of the American Statistical Association* **99** 990–1001. [2](#), [12](#)
- OLKIN, I. and SAMPSON, A. R. (1972). Jacobians of matrix transformations and induced functional equations. *Linear Algebra and its applications* **5** 257–276. [11](#)
- PETRONE, S., GUINDANI, M. and GELFAND, A. E. (2009). Hybrid Dirichlet mixture models for functional data. *Journal of the Royal Statistical Society: Series B (Statistical Methodology)* **71** 755–782. [6](#)
- RAO, J. S. (2023). *Statistical Methods in Health Disparity Research*. Chapman & Hall/CRC, Boca Raton, FL. [1](#), [19](#)
- RODRÍGUEZ, A., DUNSON, D. B. and GELFAND, A. E. (2010). Latent stick-breaking processes. *Journal of the American Statistical Association* **105** 647–659. [6](#)

- SHI, W.-X. and CHEN, S.-Q. (2004). Frequencies of poor metabolizers of cytochrome P450 2C19 in esophagus cancer, stomach cancer, lung cancer and bladder cancer in Chinese population. *World journal of gastroenterology: WJG* **10** 1961. 3
- SUN, W., REICH, B. J., TONY CAI, T., GUINDANI, M. and SCHWARTZMAN, A. (2015). False discovery control in large-scale spatial multiple testing. *Journal of the Royal Statistical Society Series B: Statistical Methodology* **77** 59–83. 12
- VATS, D., FLEGAL, J. M. and JONES, G. L. (2019). Multivariate output analysis for Markov chain Monte Carlo. *Biometrika* **106** 321–337. 24
- WALLER, L. and CARLIN, B. (2010). Disease Mapping. In *Handbook Of Spatial Statistics* (A. E. Gelfand, P. Diggle, P. Guttorp and M. Fuentes, eds.) 217–243. CRC Press, Boca Raton, FL. 1
- WALLER, L. A. and GOTWAY, C. A. (2004). *Applied spatial statistics for public health data* **368**. John Wiley & Sons. 1
- WATANABE, S. and OPPER, M. (2010). Asymptotic equivalence of Bayes cross validation and widely applicable information criterion in singular learning theory. *Journal of machine learning research* **11**. 14
- WOMBLE, W. H. (1951). Differential Systematics. *Science* **114** 315–322. 1
- ZHANG, Y., HODGES, J. S. and BANERJEE, S. (2009). Smoothed ANOVA with Spatial Effects as A Competitor to MCAR in Multivariate Spatial Smoothing. *The Annals of Applied Statistics* **3** 1805. 9

APPENDIX A: COMPUTATIONAL DETAILS

Our models rely on posterior inference, which is achieved through MCMC posterior simulations. To accomplish this, we employ the blocked Gibbs Sampler with some adaptive and some classic Metropolis-Hastings steps, based on the work by [Gamerman and Lopes \(2006\)](#) and [Miasojedow, Moulines and Vihola \(2013\)](#). We decided not to employ an adaptive strategy for γ due to its high-dimensionality and for \mathbf{A} due to the particular sampling step involving it. This approach allows us to achieve the desired acceptance rates while updating all random parameters in our model. It is important to note that ϕ_i corresponds to θ_{u_i} , and we update ϕ_i by updating both θ and u_i , and, ultimately, that η is constrained to be between 0 and a positive constant M . The MCMC algorithm proceeds through the following steps, with a noteworthy observation that step 8 is further subdivided into three parts, depending on the selected model used to represent disease dependence.

Algorithm 1: Posterior inference of θ , β , τ_s , \mathbf{V} , γ , ρ , η and \mathbf{A} or α or ρ_{dis} based on our models

1: update $\beta \mid \theta$

(a) sample candidate β^* from $\mathcal{N}(\beta, \xi_\beta)$

(b) accept β^* with probability

$$\min \left\{ 1, \frac{\exp \left(\sum_{k=1}^K \sum_{i,d:\phi_{id}=\theta_k} y_{id} (\mathbf{x}_{id}^T \beta_d^* + \phi_{id}) - E_{id} \exp (\mathbf{x}_{id}^T \beta_d^* + \phi_{id}) - \frac{\beta_d^{*T} \beta_d^*}{2\sigma_\beta^2} \right)}{\exp \left(\sum_{k=1}^K \sum_{i,d:\phi_{id}=\theta_k^*} y_{id} (\mathbf{x}_{id}^T \beta_d + \phi_{id}) - E_{id} \exp (\mathbf{x}_{id}^T \beta_d + \phi_{id}) - \frac{\beta_d^T \beta_d}{2\sigma_\beta^2} \right)} \right\}$$

(c) adapt ξ_β

2: update $\theta | \beta, \tau_s$

- (a) sample candidate θ^* from $\mathcal{N}(\theta, \xi_\theta)$
- (b) accept θ^* with probability

$$\min \left\{ 1, \frac{\exp \left(\sum_{k=1}^K \sum_{i,d:\phi_{id}=\theta_k^*} y_{id}(\mathbf{x}_{id}^T \beta_d + \phi_{id}) - E_{id} \exp(\mathbf{x}_{id}^T \beta_d + \phi_{id}) - \frac{\theta_k^{*2}}{2} \tau_s \right)}{\exp \left(\sum_{k=1}^K \sum_{i,d:\phi_{id}=\theta_k} y_{id}(\mathbf{x}_{id}^T \beta_d + \phi_{id}) - E_{id} \exp(\mathbf{x}_{id}^T \beta_d + \phi_{id}) - \frac{\theta_k^2}{2} \tau_s \right)} \right\}$$

(c) adapt ξ_θ

3: update $\gamma_{id} | \beta, \theta, \rho, \eta, \mathbf{A}, i = 1, \dots, n, d = 1, \dots, q$

- (a) sample candidate γ_{id}^* from $\mathcal{N}(\gamma_{id}, \xi_\gamma)$
- (b) compute the corresponding candidate $u_{id}^* = \sum_{k=1}^K kI \left(\sum_{t=1}^{k-1} p_t < F^{(id)}(\gamma_{id}^*) < \sum_{t=1}^k p_t \right)$
- (c) accept γ_{id}^* with probability

$$\min \left\{ 1, \frac{\exp \left(y_{id}(\mathbf{x}_{id}^T \beta_d + \theta_{u_{id}^*}) - E_i \exp(\mathbf{x}_{id}^T \beta_d + \theta_{u_{id}^*}) - \frac{\gamma^{*T} \Sigma_\gamma^{-1} \gamma^*}{2} \right)}{\exp \left(y_{id}(\mathbf{x}_{id}^T \beta_d + \theta_{u_{id}}) - E_{id} \exp(\mathbf{x}_{id}^T \beta_d + \theta_{u_{id}}) - \frac{\gamma^T \Sigma_\gamma^{-1} \gamma}{2} \right)} \right\}$$

4: update $\mathbf{V} | \beta, \theta$

- (a) let $\tilde{\mathbf{V}} = \text{logit}(\mathbf{V})$ and sample $\tilde{\mathbf{V}}^*$ from $\mathcal{N}(\tilde{\mathbf{V}}, \xi_{\tilde{\mathbf{V}}})$ then $\mathbf{V}^* = \frac{\exp(\tilde{\mathbf{V}}^*)}{1 + \exp(\tilde{\mathbf{V}}^*)}$
- (b) compute the corresponding candidate $\mathbf{p}^* = (p_1^*, \dots, p_K^*)$ and $\mathbf{u} = \{u_{id}^*\}$
- (c) accept \mathbf{V}^* with probability

$$\min \left\{ 1, \frac{\exp \left(\sum_{i,d} y_{id}(\mathbf{x}_{id}^T \beta_d + \theta_{u_{id}^*}) - E_{id} \exp(\mathbf{x}_{id}^T \beta_d + \theta_{u_{id}^*}) \right) \prod_{k=1}^K (1 - V_k^*)^{(\alpha-1)} \prod_{k=1}^K V_k^* (1 - V_k^*)}{\exp \left(\sum_{i,d} y_{id}(\mathbf{x}_{id}^T \beta_d + \theta_{u_{id}}) - E_{id} \exp(\mathbf{x}_{id}^T \beta_d + \theta_{u_{id}}) \right) \prod_{k=1}^K (1 - V_k)^{(\alpha-1)} \prod_{k=1}^K V_k (1 - V_k)} \right\}$$

(d) adapt $\xi_{\tilde{\mathbf{V}}}$

5: sample $\tau_s | \theta, \beta_0$ from

$$\Gamma \left(a_s + \frac{K}{2}, b_s + \frac{\sum_{k=1}^K \theta_k^2}{2} \right)$$

6: update $\rho | \gamma, \eta, \mathbf{A}$

- (a) let $\tilde{\rho} = \text{logit}(\rho)$ and sample $\tilde{\rho}^*$ from $\mathcal{N}(\tilde{\rho}, \xi_{\tilde{\rho}})$ then $\rho^* = \frac{\exp(\tilde{\rho}^*)}{1 + \exp(\tilde{\rho}^*)}$
- (b) update Σ_γ^* with the proposed ρ^*
- (c) accept $\tilde{\rho}^*$ with probability

$$\min \left\{ 1, \frac{|\Sigma_\gamma^*|^{-\frac{N}{2}} \exp \left(-\frac{\gamma^T \Sigma_\gamma^{*-1} \gamma}{2} \right) \prod_{d=1}^q \rho_d^* (1 - \rho_d^*)}{|\Sigma_\gamma|^{-\frac{N}{2}} \exp \left(-\frac{\gamma^T \Sigma_\gamma^{-1} \gamma}{2} \right) \prod_{d=1}^q \rho_d (1 - \rho_d)} \right\}$$

(d) adapt $\xi_{\tilde{\rho}}$

7: update $\eta | \gamma, \rho, \mathbf{A}$

- (a) let $\tilde{\eta} = \log \left(\frac{\eta}{M - \eta} \right)$ and sample $\tilde{\eta}^*$ from $\mathcal{N}(\tilde{\eta}, \xi_{\tilde{\eta}})$ then $\eta^* = \frac{M \exp(\tilde{\eta}^*)}{1 + \exp(\tilde{\eta}^*)}$
- (b) update Σ_γ^* with the proposed η^*
- (c) accept $\tilde{\eta}^*$ with probability

$$\min \left\{ 1, \frac{|\Sigma_\gamma^*|^{-\frac{N}{2}} \exp \left(-\frac{\gamma^T \Sigma_\gamma^{*-1} \gamma}{2} \right) \prod_{d=1}^q \frac{\exp(\tilde{\eta}_d^*)}{(1 + \exp(\tilde{\eta}_d^*))^2}}{|\Sigma_\gamma|^{-\frac{N}{2}} \exp \left(-\frac{\gamma^T \Sigma_\gamma^{-1} \gamma}{2} \right) \prod_{d=1}^q \frac{\exp(\tilde{\eta}_d)}{(1 + \exp(\tilde{\eta}_d))^2}} \right\}$$

(d) adapt $\xi_{\tilde{\eta}}$

8: **Unstructured** update $\mathbf{A} \mid \gamma, \rho, \eta$

- (a) let $\tilde{a}_{dd} = \log(a_{dd})$ and sample candidates \tilde{a}_{dd}^* from $\mathcal{N}(\tilde{a}_{dd}, \xi_{\tilde{a}})$
- (b) for off-diagonal elements a_{dh} , $d \neq h$, a_{dh}^* are sampled from $\mathcal{N}(\tilde{a}_{dh}, \xi_a)$
- (c) update Σ_γ^* with the proposed \mathbf{A}^*
- (d) accept \mathbf{A}^* with probability

$$\min \left\{ 1, \frac{|\Sigma_\gamma^*|^{-\frac{N}{2}} \exp\left(-\frac{\gamma^T \Sigma_\gamma^{*-1} \gamma}{2}\right) p(\mathbf{A}^*) \prod_{d=1}^q a_{dd}^*}{|\Sigma_\gamma|^{-\frac{N}{2}} \exp\left(-\frac{\gamma^T \Sigma_\gamma^{-1} \gamma}{2}\right) p(\mathbf{A}) \prod_{d=1}^q a_{dd}} \right\}$$

Directed sample $\alpha_d \mid \gamma, \rho_d$ from

$$\mathcal{N}(\mathbf{H}_d h_d, H_d)$$

where $\mathbf{H}_d = (\delta_d^T Q_d \delta_d + \Sigma_\alpha^{-1})^{-1}$ and $h_d = \delta_d^T Q_d \gamma_d + \Sigma_\alpha^{-1} \mu_\alpha$. Here $\delta_d = (F_h)_{h \in N_d}$, $F_h = (\gamma_h, \zeta_h)$, $N_d = \{h : h \sim d, h < d\}$ and $\zeta_h = (\sum_{j \sim 1} \gamma_{h,j}, \dots, \sum_{j \sim n} \gamma_{h,j})$. Then update $\mathbf{A}_{d,h}$ matrices and consequently Σ_γ .

Undirected update $\rho_{dis} \mid \gamma, \rho, \eta$

- (a) let $\tilde{\rho}_{dis} = \log\left(\frac{\rho_{dis} + 1}{1 - \rho_{dis}}\right)$ and sample $\tilde{\rho}_{dis}^*$ from $\mathcal{N}(\tilde{\rho}_{dis}, \xi_{\tilde{\rho}_{dis}})$ then $\rho_{dis}^* = \frac{\exp(\tilde{\rho}_{dis}^*) - 1}{1 + \exp(\tilde{\rho}_{dis}^*)}$
- (b) update Λ_{dis}^* with the proposed ρ_{dis}^* and then Σ_γ^*
- (c) accept $\tilde{\rho}_{dis}^*$ with probability

$$\min \left\{ 1, \frac{|\Sigma_\gamma^*|^{-\frac{N}{2}} \exp\left(-\frac{\gamma^T \Sigma_\gamma^{*-1} \gamma}{2}\right) \frac{\exp(\tilde{\rho}_{dis}^*)}{(1 + \exp(\tilde{\rho}_{dis}^*))^2}}{|\Sigma_\gamma|^{-\frac{N}{2}} \exp\left(-\frac{\gamma^T \Sigma_\gamma^{-1} \gamma}{2}\right) \frac{\exp(\tilde{\rho}_{dis})}{(1 + \exp(\tilde{\rho}_{dis}))^2}} \right\}$$

- (d) adapt $\xi_{\tilde{\rho}_{dis}}$

APPENDIX B: MARKOV CHAIN MONTE CARLO STANDARD ERROR

Monte Carlo estimates, whether for MCMC output or any other purpose, should always be accompanied by Monte Carlo standard error. This means that if the central limit theorem applies, the corresponding covariance matrices' estimates must be reported, either directly or indirectly. Due to the correlation between the obtained samples, these quantities necessitate more advanced tools compared to typical sample estimators. It's important to note that the validity of a Markov chain central limit theorem is not guaranteed in all cases, as it depends on the convergence rate of the Markov chain. Nonetheless, this assumption is also made when employing various convergence diagnostics. In this context, we present the estimates, by using `mcmcse` R package (Flegal et al., 2021), of the standard error and the effective sample size, based on Gong and Flegal (2016), to demonstrate that we can maintain control over the Monte Carlo error by applying a predefined threshold Vats, Flegal and Jones (2019).

Table 3 presents the estimates of the highest level of the parameters hierarchy. Additionally, the Monte Carlo standard error is reported, revealing that the highest value is 0.059, the only one surpassing the standard threshold of 0.05.

Next, we provide the multivariate effective sample size of the chain, computed as 1940.335 using the formula $B \frac{|\Lambda|^{1/p}}{|\Sigma|^{1/p}}$. Here, B is the total number of iterations post burn-in, Λ represents the sample covariance matrix, and Σ is an estimate of the Monte Carlo standard error. This computation accounts for the multivariate dependence structure of the process. Comparing our effective sample size to the minimum requirement of 7619 for achieving a precision level

TABLE 3
Estimates and Monte Carlo standard errors for the high level parameters of the hierarchy

Variable	Estimate	Standard Error
β_0	0.046	0.001
τ_s	6.830	0.012
θ_1	0.217	0.001
θ_2	0.344	0.002
θ_3	0.042	0.001
θ_4	-0.022	0.008
θ_5	0.109	0.002
θ_6	-0.067	0.001
θ_7	0.004	0.006
θ_8	-0.145	0.018
θ_9	-0.057	0.005
θ_{10}	-0.062	0.022
θ_{11}	0.398	0.042
θ_{12}	0.268	0.059
θ_{13}	-0.011	0.012
θ_{14}	-0.169	0.015
θ_{15}	-0.137	0.002

relative to the variability in the target distribution of 0.05, we observe that ours is significantly lower. However, it is important to note that we computed the precision level of our estimate, obtained with an estimated effective sample size of 1940.335, which amounts to 0.099. This precision level is higher than 0.05 but lower than 0.1.

APPENDIX C: ADDITIONAL FIGURES AND TABLES



Fig 12: California map with county names labeled

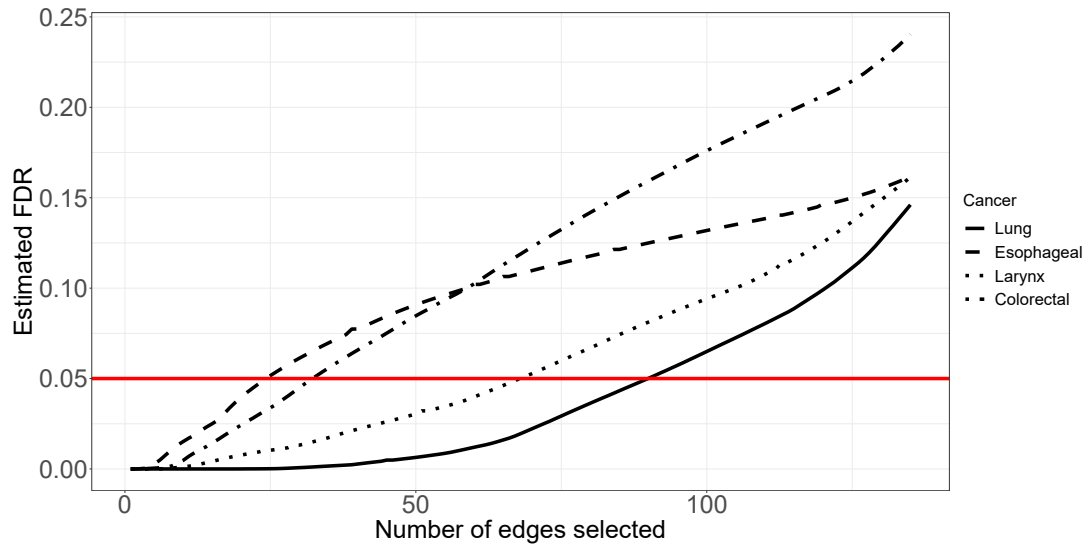


Fig 13: Estimated FDR curves plotted against the number of selected difference boundaries for four cancers in the case study with covariates only in the adjacency model

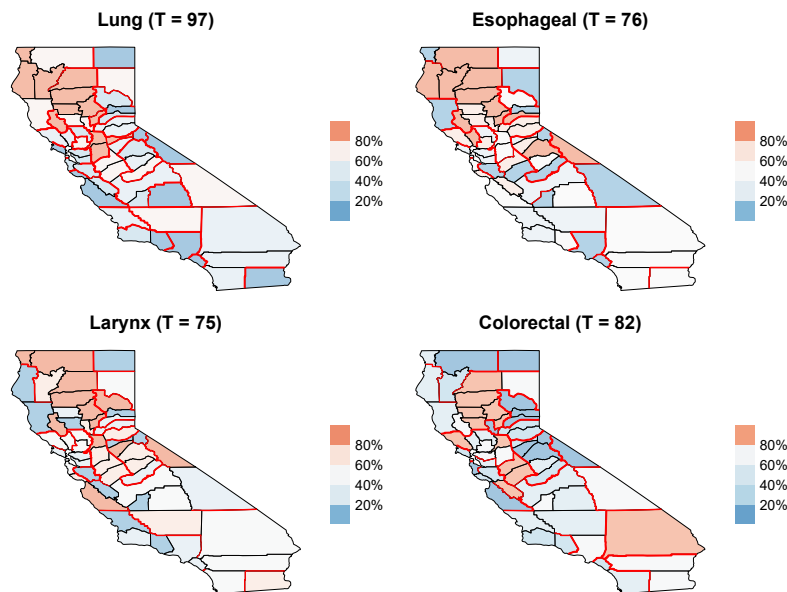


Fig 14: Difference boundaries (highlighted in red) detected by the model, in the case study with covariates only in the adjacency model, in SIR map for four cancers individually when $\zeta = 0.05$. The values in brackets are the number of difference boundaries detected.

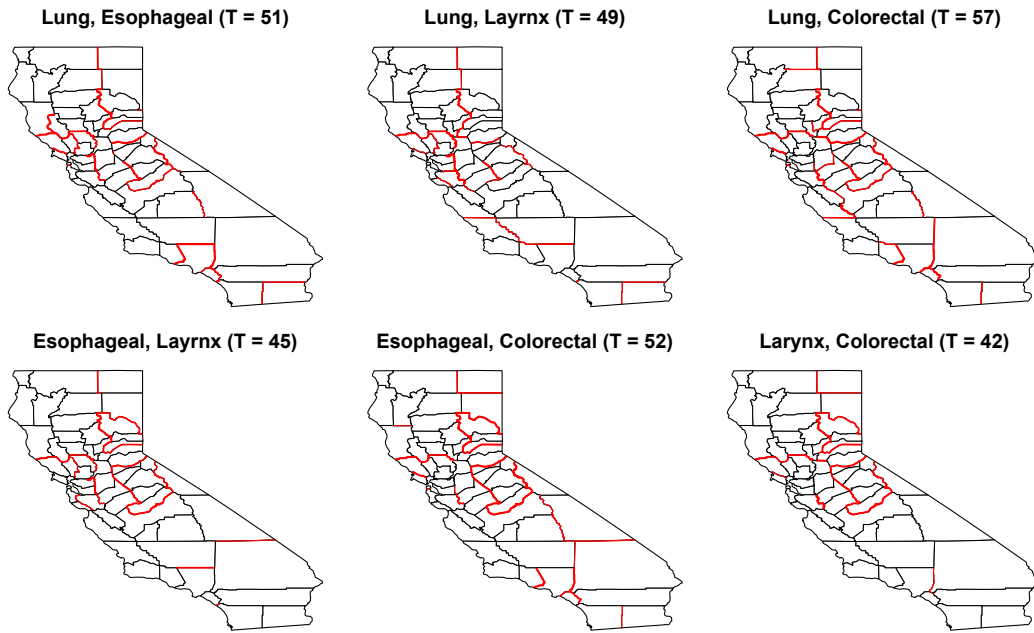


Fig 15: Shared difference boundaries (highlighted in red) detected by the model, in the case study with covariates only in the adjacency model, for each pair of cancers in SIR map when $\zeta = 0.05$. The values in brackets are the number of difference boundaries detected.

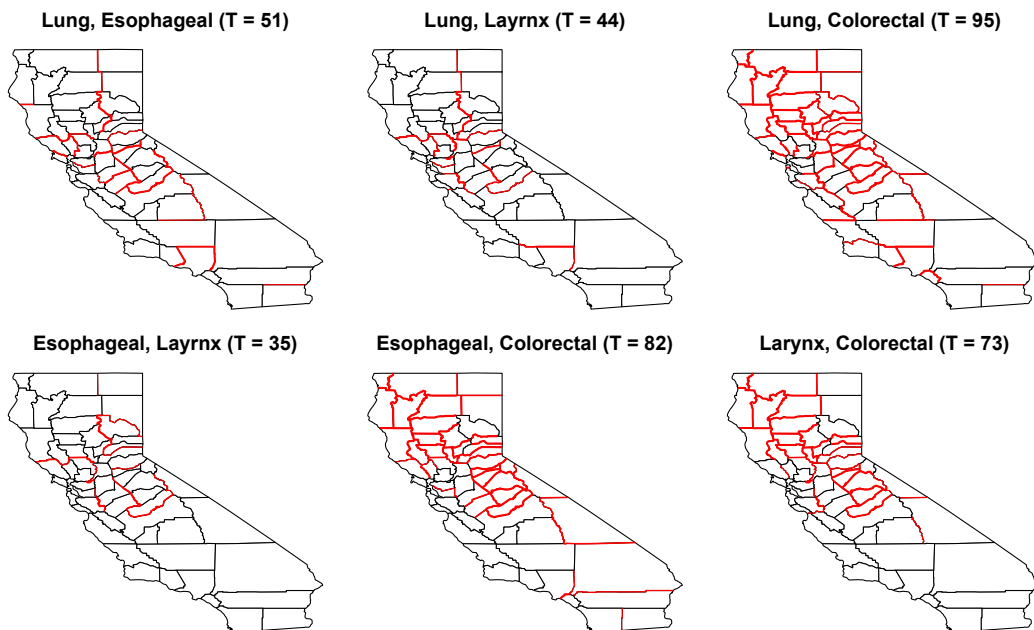


Fig 16: Mutual cross-difference boundaries (highlighted in red) detected by the model, in the case study with covariates only in the adjacency model, for each pair of cancers in SIR map when $\zeta = 0.05$. The values in brackets are the number of difference boundaries detected.

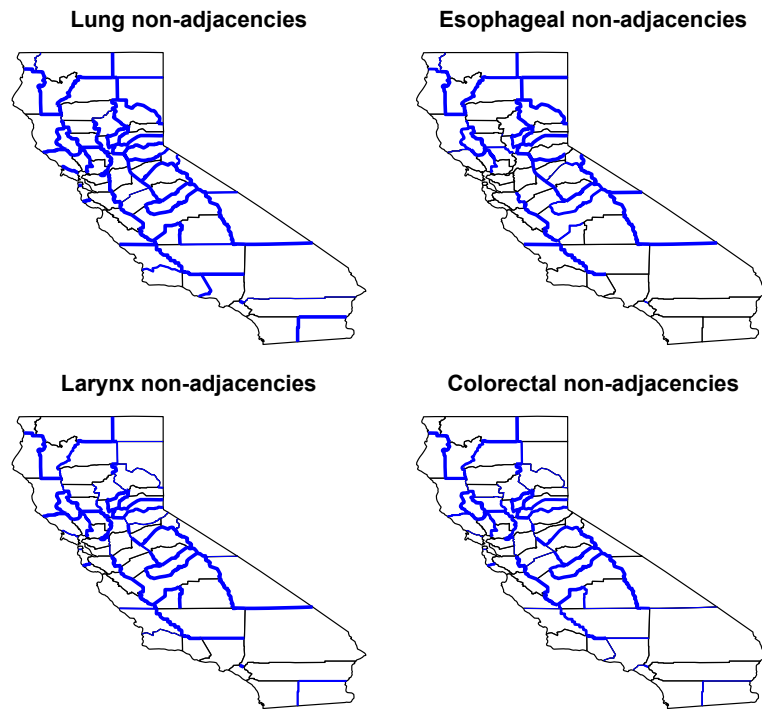


Fig 17: Non-adjacencies (shown in blue), in the case study with covariates only in the adjacency model, overlaid on smoking rates. The thickness of the lines is proportional to the probability of being considered as a non-adjacency

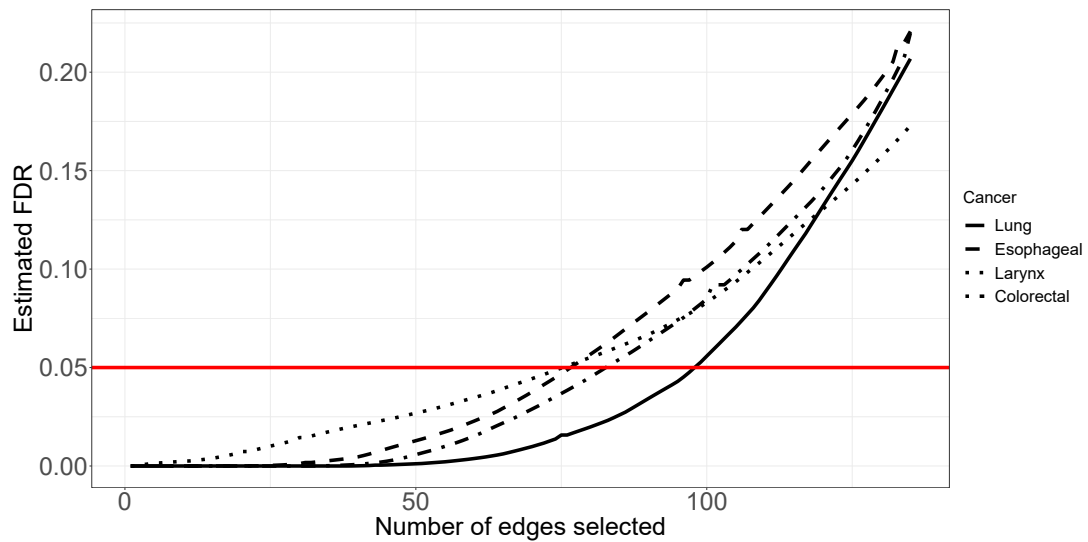


Fig 18: Estimated FDR curves plotted against the number of selected difference boundaries for four cancers in the case study with covariates only in the mean with fixed adjacencies

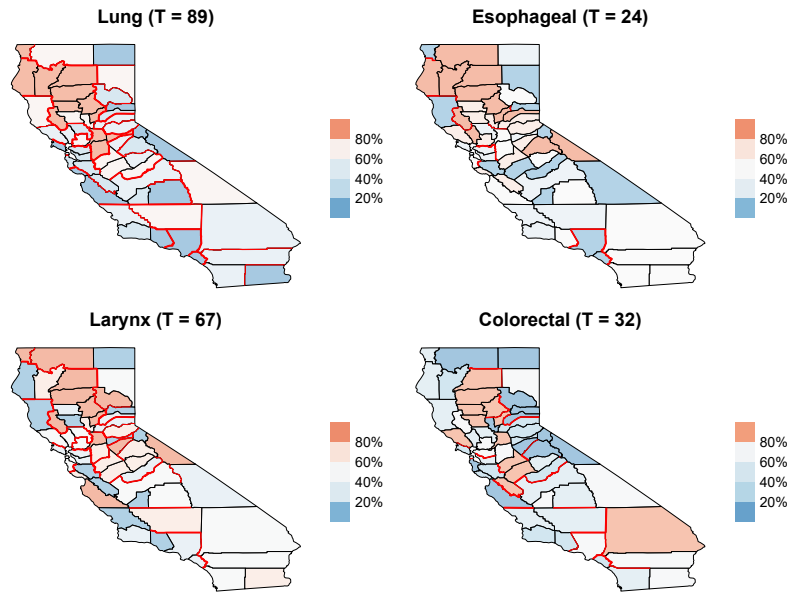


Fig 19: Difference boundaries (highlighted in red) detected by the model, in the case study with covariates only in the mean with fixed adjacencies, in SIR map for four cancers individually when $\zeta = 0.05$. The values in brackets are the number of difference boundaries detected.

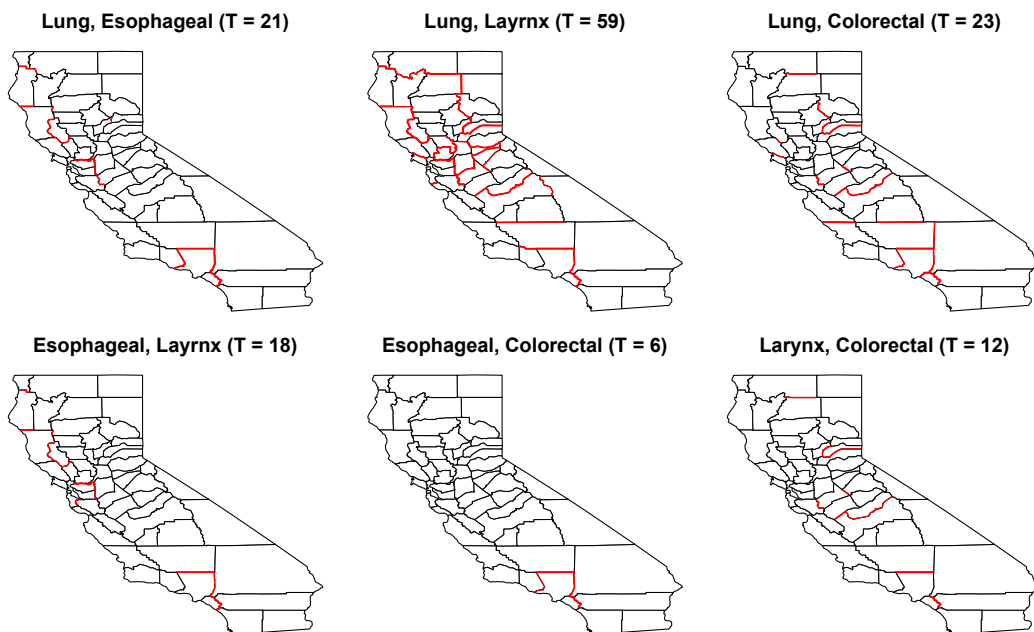


Fig 20: Shared difference boundaries (highlighted in red) detected by the model, in the case study with covariates only in the mean with fixed adjacencies, for each pair of cancers in SIR map when $\zeta = 0.05$. The values in brackets are the number of difference boundaries detected.

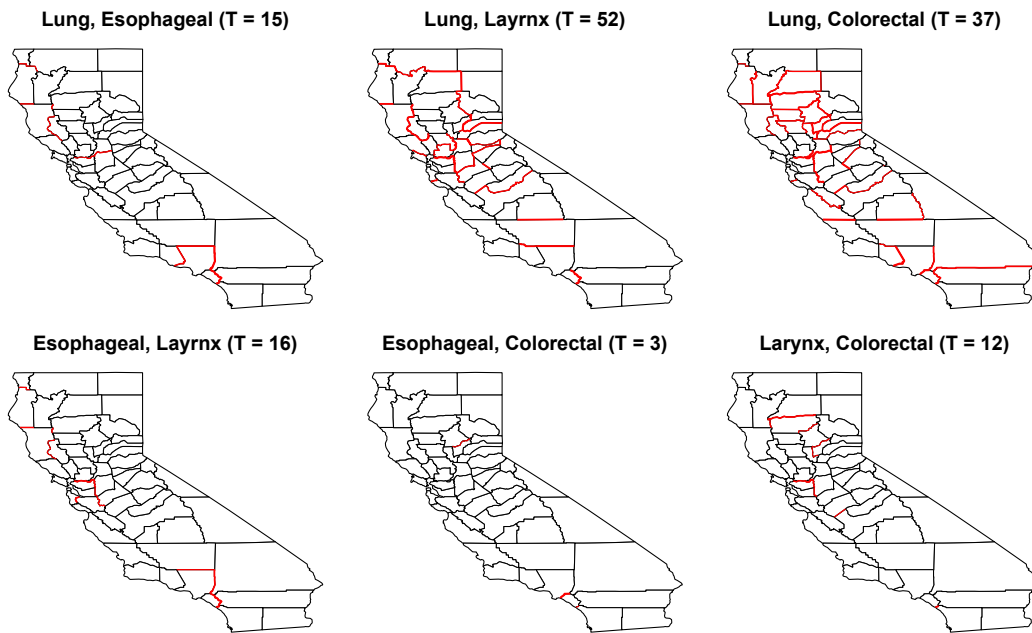


Fig 21: Mutual cross-difference boundaries (highlighted in red) detected by the model, in the case study with covariates only in the mean with fixed adjacencies, for each pair of cancers in SIR map when $\zeta = 0.05$. The values in brackets are the number of difference boundaries detected.

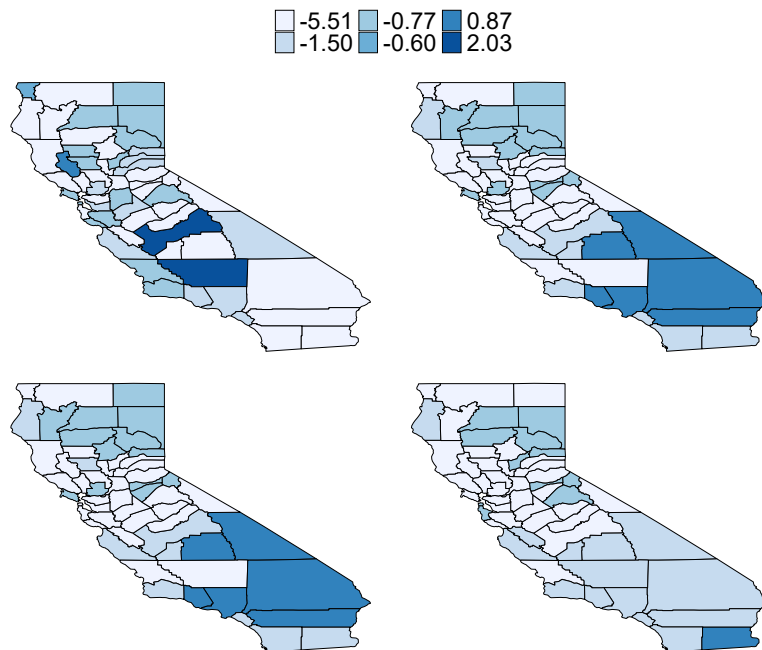


Fig 22: Simulated data maps depicting the random effects for the four cancers using a disease directed graph.

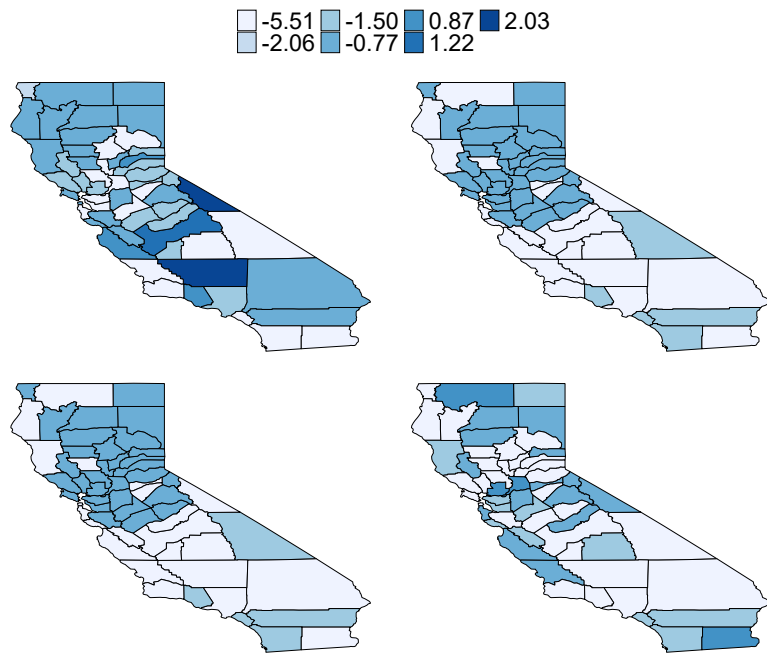


Fig 23: Simulated data maps depicting the random effects for the four cancers using a disease undirected graph.

Table 4: Sensitivities and specificities for boundary detection across diseases

Disease graph	T	1 vs 2		2 vs 1		1 vs 3		3 vs 1		1 vs 4		4 vs 1		2 vs 3		3 vs 2		2 vs 4		4 vs 2		3 vs 4		4 vs 3	
		Spec	Sens	Spec																					
Unstructured	80	0.514	0.611	0.176	0.885	0.517	0.618	0.466	0.596	0.478	0.604	0.410	0.572	0.565	0.664	0.602	0.655	0.457	0.601	0.443	0.589	0.443	0.591	0.422	0.577
	90	0.445	0.681	0.176	0.885	0.433	0.685	0.399	0.672	0.412	0.677	0.348	0.646	0.477	0.720	0.513	0.720	0.391	0.673	0.370	0.659	0.378	0.663	0.350	0.647
	100	0.358	0.748	0.176	0.885	0.357	0.755	0.321	0.740	0.334	0.746	0.284	0.724	0.390	0.784	0.411	0.779	0.310	0.740	0.303	0.734	0.300	0.732	0.285	0.723
	110	0.263	0.811	0.176	0.885	0.270	0.819	0.238	0.807	0.243	0.811	0.219	0.798	0.298	0.844	0.310	0.838	0.234	0.808	0.229	0.806	0.215	0.796	0.213	0.796
	120	0.165	0.873	0.176	0.885	0.185	0.885	0.150	0.876	0.157	0.874	0.139	0.865	0.199	0.900	0.205	0.895	0.158	0.876	0.155	0.875	0.139	0.865	0.140	0.867
Directed	80	0.451	0.606	0.114	0.860	0.436	0.633	0.436	0.617	0.442	0.607	0.428	0.584	0.526	0.746	0.573	0.783	0.434	0.604	0.443	0.612	0.419	0.587	0.418	0.572
	90	0.376	0.664	0.114	0.860	0.364	0.685	0.379	0.683	0.374	0.669	0.352	0.648	0.444	0.802	0.483	0.830	0.369	0.669	0.371	0.680	0.352	0.648	0.350	0.647
	100	0.294	0.733	0.114	0.860	0.300	0.755	0.309	0.748	0.297	0.737	0.276	0.717	0.361	0.856	0.397	0.883	0.288	0.733	0.298	0.746	0.274	0.715	0.279	0.716
	110	0.221	0.801	0.114	0.860	0.223	0.814	0.227	0.811	0.220	0.803	0.213	0.796	0.273	0.899	0.299	0.921	0.217	0.804	0.224	0.816	0.199	0.779	0.202	0.776
	120	0.144	0.871	0.114	0.860	0.145	0.875	0.144	0.871	0.144	0.871	0.135	0.863	0.181	0.938	0.201	0.954	0.143	0.876	0.144	0.876	0.129	0.857	0.131	0.852
Undirected	80	0.406	0.582	0.155	0.876	0.469	0.596	0.425	0.577	0.430	0.580	0.434	0.582	0.518	0.651	0.570	0.647	0.394	0.573	0.399	0.575	0.444	0.597	0.426	0.592
	90	0.338	0.650	0.155	0.876	0.382	0.661	0.344	0.648	0.343	0.647	0.360	0.654	0.429	0.705	0.508	0.712	0.328	0.642	0.326	0.640	0.371	0.663	0.349	0.655
	100	0.274	0.722	0.155	0.876	0.308	0.732	0.264	0.718	0.270	0.718	0.288	0.724	0.340	0.760	0.417	0.773	0.254	0.711	0.266	0.715	0.306	0.736	0.287	0.727
	110	0.202	0.792	0.155	0.876	0.217	0.798	0.197	0.789	0.203	0.792	0.221	0.798	0.257	0.821	0.331	0.834	0.189	0.783	0.208	0.794	0.230	0.803	0.209	0.795
	120	0.140	0.867	0.155	0.876	0.133	0.864	0.135	0.864	0.126	0.862	0.146	0.871	0.173	0.885	0.234	0.897	0.120	0.857	0.137	0.866	0.163	0.877	0.145	0.869